

LHC Higgs Signatures from Extended Electroweak Gauge Symmetry

Tomohiro Abe,^a Ning Chen,^a Hong-Jian He^{a,b,c}

^a*Institute of Modern Physics and Center for High Energy Physics,
Tsinghua University, Beijing 100084, China*

^b*Center for High Energy Physics, Peking University, Beijing 100871, China*

^c*Kavli Institute for Theoretical Physics China, CAS, Beijing 100190, China*

E-mail: tomohiro_abe@tsinghua.edu.cn, hep_nchen@tsinghua.edu.cn,
hjhe@tsinghua.edu.cn

ABSTRACT:

We study LHC Higgs signatures from the extended electroweak gauge symmetry $SU(2) \otimes SU(2) \otimes U(1)$. Under this gauge structure, we present an effective UV completion of the 3-site moose model with ideal fermion delocalization, which contains two neutral Higgs states (h , H) plus three new gauge bosons (W' , Z'). We study the unitarity, and reveal that the exact E^2 cancellation in the longitudinal $V_L V_L$ scattering amplitudes is achieved by the joint role of exchanging both spin-1 new gauge bosons and spin-0 Higgs bosons. We identify the lighter Higgs state h with mass 125 GeV, and derive the unitarity bound on the mass of heavier Higgs boson H . The parameter space of this model is highly predictive. We study the production and decay signals of this 125 GeV Higgs boson h at the LHC. We demonstrate that the h Higgs boson can naturally have enhanced signals in the diphoton channel $gg \rightarrow h \rightarrow \gamma\gamma$, while the event rates in the reactions $gg \rightarrow h \rightarrow WW^*$ and $gg \rightarrow h \rightarrow ZZ^*$ are generally suppressed relative to the SM expectation. Searching the h Higgs boson via the associated production and the vector boson fusions are also discussed for our model. We further analyze the LHC signals of the heavier Higgs boson H as a new physics discriminator from the SM. For wide mass-ranges of H , we derive constraints from the existing LHC searches, and study the discovery potential of H at the LHC (8 TeV) and LHC (14 TeV).

KEYWORDS: Higgs Physics, Beyond Standard Model

JHEP (2012), in Press [arXiv:1207.4103]

Contents

1 Introduction	3
2 Spontaneous Symmetry Breaking and Unitarity	5
2.1 Structure of the 221 Model	5
2.2 Higgs Sector of the Model	8
2.3 Fermion Sector of the Model	9
2.4 Couplings of Higgs Bosons, Gauge Bosons and Fermions	11
2.4.1 Gauge and Yukawa Couplings of Higgs Bosons	11
2.4.2 Gauge Boson Self-Couplings and Gauge-Fermion Couplings	13
2.5 Unitarity: Roles of Spin-1 Gauge Bosons versus Spin-0 Higgs Bosons	14
3 LHC Signatures of the Lighter Higgs Boson h^0	21
3.1 Decay Branching Fractions of h^0	21
3.2 Signatures of h^0 via Gluon Fusion	23
3.3 Signatures of h^0 via Associated Production and Vector Boson Fusion	28
4 LHC Signatures of the Heavier Higgs Boson H^0	29
4.1 Decay Branching Fractions and Productions of H^0	30
4.2 LHC Potential of Detecting H^0	33
5 Conclusions	39
Acknowledgments	40
A Decays of the Lighter Higgs Boson	40
B Decays of the Heavier Higgs Boson	45
References	46

1 Introduction

The excellent performance of the LHC running at 7 TeV (2011) and 8 TeV (2012) has allowed both ATLAS and CMS collaborations to explore substantial mass-ranges of the Higgs boson [1] in the standard model (SM) [2]. During 2011 and the first half of 2012, each collaboration has collected about 10 fb^{-1} data. The planned LHC running in 2012 is extended for seven weeks until December 16, 2012, and will accumulate up to 20 fb^{-1} data in each detector. So far ATLAS has excluded the SM Higgs mass-range up to 523 GeV at 99% C.L., except the small window of (120.8, 130.7) GeV [3]. At the meantime, CMS excluded the SM Higgs mass-ranges of (110, 112) GeV, (113, 121.5) GeV and (128, 600) GeV at 99% C.L. [4]. Both experiments have detected exciting event excesses around the mass window of 125–126 GeV [5, 6]: ATLAS reached a 5.9σ significance at 126.0 GeV and CMS deduced a 5.0σ signal at 125.3 GeV. These are obtained by combining the most sensitive search channels of $(\gamma\gamma, WW^*, ZZ^*)$. With the combined data from $7 \oplus 8$ TeV collisions, the ratios of the observed ATLAS and CMS signals over the SM expectations in the $\gamma\gamma$ decay mode are 1.8 ± 0.5 and $1.5_{-0.3}^{+0.6}$, respectively. For the $ZZ^* \rightarrow 4\ell$ decay channel, the experiments have the observed rates over the SM expectations equal 1.2 ± 0.6 [ATLAS] and $0.7_{-0.4}^{+0.6}$ [CMS]. In the $WW^* \rightarrow \ell\nu\ell\nu$ channel, the observed rates relative to the SM are 1.3 ± 0.5 [ATLAS] and 0.6 ± 0.4 [CMS]. For the $b\bar{b}$ and $\tau\bar{\tau}$ final states, the data still have large statistic errors and the central values fall in between zero and the SM expectations. — It is intriguing that the current observed Higgs signals in the diphoton mode are found to be always higher than the SM values, which is an indication of possible new physics in the electroweak symmetry breaking mechanism.

Extending the SM gauge symmetry is a fundamental way to construct new physics beyond the SM. This is especially motivated by the deconstruction [7] approach of the electroweak symmetry breaking [8–10], which includes additional SU(2) and/or U(1) gauge groups. Such extra gauge groups are also generic in the low energy theories of many unified models [11]. In this work, we consider the minimal gauge extension of the SM with an extra SU(2) gauge group, which will be called 221 model for abbreviation. We will focus on its Higgs sector for the desired gauge symmetry breaking $SU(2)_0 \otimes SU(2)_1 \otimes U(1)_2 \rightarrow U(1)_{\text{em}}$. This can be viewed as an effective UV completion of the nonlinearly realized 3-site Higgsless moose model [9] by adding two Higgs doublets Φ_1 and Φ_2 . After the spontaneous symmetry breaking, two Higgs doublets give rise to six would-be Goldstone bosons for the mass generation of six gauge bosons (W_0^a, W_1^a) , and leave two neutral Higgs states (h^0, H^0) in the physical particle spectrum.¹ The gauge sector of our 221 model is the same as the 3-site moose model [9] or the nonlinear BESS model [12] and the hidden local symmetry model [13]. Our fermion sector follows the 3-site model [9], where the fermions enjoy the ideal delocalization [14]. This makes the new weak gauge bosons essentially fermiophobic, so they can be relatively light and significantly below 1 TeV. The ideal delocalization minimizes the electroweak corrections to the oblique parameters, and gives the leading contributions to the triple gauge coupling of WWZ , where

¹Here, two Higgs VEVs are equal [9] or of the same order of magnitudes, different from all other types of extended $SU(2) \otimes SU(2) \otimes U(1)$ models in the literature.

(W, Z) denote the light weak gauge bosons. The LEP-II constraint was found to only put a mild lower limit on the new gauge boson mass of W' to be about 300 GeV [9, 10]; it also escapes from the current direct searches at the LHC and Tevatron [15]. The signatures of such new gauge bosons were studied at the LHC (8 TeV) and LHC (14 TeV), which have good discovery potential over the wide gauge boson mass-range of 250 GeV–1 TeV [16]. We also note that realizing the ideal delocalization [14] adds additional vector-like fermions, which will contribute to loop-induced processes for both Higgs productions and decays (cf. Appendix). The phenomenologies of the pure gauge and fermion sectors of our 221 model are mainly the same as the 3-site moose model [9].²

The goal of the present work is to focus on the full Higgs sector of the 221 model and its LHC signatures, which were not available before. In section 2, we first set up the model, including the gauge and Yukawa interactions of the two Higgs doublets, and the complete Higgs potential. Then, we present the non-standard couplings of Higgs bosons to all gauge bosons and fermions, including the new gauge bosons W'/Z' and the heavy vector-like fermions F . In particular, the coupling strengths between the light Higgs boson h^0 and the light weak bosons W/Z are generically reduced relative to those of the SM Higgs boson. We further study the LHC signals of the heavier Higgs boson H^0 whose discovery will play the key role to discriminate the present model from the SM. In addition, we analyze the perturbative unitarity condition of our model, and reveal that the exact E^2 cancellation in the longitudinal $V_L V_L$ scattering amplitudes is achieved by *the joint role of exchanging both spin-1 new gauge bosons (W', Z') and spin-0 Higgs bosons (h, H)*. Identifying the lighter Higgs boson h^0 with mass of 125 GeV, we derive the unitarity bound on the mass of heavier Higgs state H^0 .

In section 3, we systematically analyze the LHC signatures of the lighter Higgs boson h^0 with mass of $M_h = 125$ GeV. The dominant gluon-fusion processes are shown to be mostly sensitive to the Higgs mixing angle α , and the Higgs production cross section can be enhanced over the SM expectation due to the new heavy quark contributions of our model. The sub-dominant processes of vector boson fusion (VBF) and the Higgs associated productions are also studied, which always predict suppressed signals relative to the SM Higgs boson. Combining the analyses of both productions and decays, we demonstrate that our model can generate the observed di-photon signals in proper parameter regions. On the other hand, we will show that h^0 signals from the WW^*/ZZ^* channels are always suppressed, and are consistent with the current LHC data [3, 4]. No excess of Higgs signals come from either the VBF process or the vector boson associated production in our model. In parallel, we analyze the LHC signatures of the heavier Higgs boson H^0 as a new physics discriminator from the SM in section 4. Due to the suppressed couplings of H^0 with the SM particles, the discovery potential of H^0 is quite challenging, but it can be further probed at the LHC (8 TeV)

²The 221 gauge group was considered in very different contexts before, such as the family non-universality model [17], the un-unified standard model [18], the topflavor seesaw model [19], and some recent collider studies [20], etc, but the Higgs sector (including the Higgs potential, mass-spectrum and couplings) and its collider phenomenology were not addressed. Their fermion sectors also substantially differ from our current setup under the ideal delocalization [14].

with more data collected by the end this year, and at the LHC (14 TeV). We also study an interesting case with h^0 and H^0 being (nearly) degenerate around mass 125 – 126 GeV. To further discover the new Higgs boson H^0 will be crucial for discriminating our 221 model from the SM.

We conclude in section 5. In addition, we provide two appendices A and B to summarize the partial decay widths for the Higgs bosons h^0 and H^0 in the 221 model, respectively.

2 Spontaneous Symmetry Breaking and Unitarity

In this section we will study the spontaneous symmetry breaking and the unitarity of the 221 model. We present the complete Higgs potential, and derive the Higgs mass-spectrum and their mixing. Afterwards, we analyze all Higgs couplings with the gauge bosons and fermions, as well as gauge boson self-couplings and gauge-fermion couplings. Finally, we study the unitarity of the present model. We reveal that the exact E^2 cancellation in the longitudinal $V_L V_L$ scattering amplitudes is achieved by the joint role of exchanging spin-1 new gauge bosons W'/Z' and spin-0 Higgs bosons. Identifying the lighter Higgs state h^0 to have mass 125 GeV, we derive the unitarity bound on the mass of heavier Higgs boson H^0 . We find that the parameter space of this model is highly predictive.

2.1 Structure of the 221 Model

We consider a minimal gauge extension of the SM with an extra $SU(2)$ gauge group, so the full electroweak gauge symmetry $\mathcal{G} = SU(2)_0 \otimes SU(2)_1 \otimes U(1)_2$ at some high energy scale will be spontaneously broken down to $U(1)_{\text{em}}$ of QED. The product gauge groups $SU(2)_0 \otimes SU(2)_1 \otimes U(1)_2$ have the gauge couplings, g_0 , g_1 , and g_2 , respectively. Since we are constructing an effective UV completion of the 3-site Higgsless nonlinear moose model [9], we will focus on the distinct parameter space $g_1 \gg (g_0, g_2)$ for the present study, which differs from most other $SU(2)$ extensions in the literature [17–20]. With $g_1 \gg (g_0, g_2)$, the $SU(2)_0 \otimes U(1)_2$ are approximately reduced to the SM electroweak gauge group $SU(2)_L \otimes U(1)_Y$, while the $SU(2)_1$ becomes the additional new gauge symmetry. We introduce two Higgs doublets Φ_1 and Φ_2 , transforming as $(\mathbf{2}, \mathbf{2}, \mathbf{0})$ and $(\mathbf{1}, \mathbf{2}, \frac{1}{2})$ under \mathcal{G} , respectively. They develop two vacuum expectation values (VEVs), f_1 and f_2 , from minimizing the Higgs potential. The gauge symmetry breaking takes in the following sequences,

$$SU(2)_0 \otimes SU(2)_1 \xrightarrow{\langle \Phi_1 \rangle \neq 0} SU(2)_V, \quad (2.1a)$$

$$SU(2)_1 \otimes U(1)_2 \xrightarrow{\langle \Phi_2 \rangle \neq 0} U(1)_V, \quad (2.1b)$$

where the subscript “ V ” represents the diagonal part of the product groups. Thus, the Lagrangian for the gauge and Higgs sectors can be written as,

$$\begin{aligned} \mathcal{L} = & -\frac{1}{4} \sum_{a=1}^3 W_{0\mu\nu}^a W_0^{a\mu\nu} - \frac{1}{4} \sum_{a=1}^3 W_{1\mu\nu}^a W_1^{a\mu\nu} - \frac{1}{4} B_{2\mu\nu} B_2^{\mu\nu} \\ & + \sum_{j=1,2} \text{tr} \left[(D_\mu \Phi_j)^\dagger (D^\mu \Phi_j) \right] - V(\Phi_1, \Phi_2), \end{aligned} \quad (2.2)$$

where $W_0^{a\mu\nu}$, $W_1^{a\mu\nu}$, and $B_2^{\mu\nu}$ are the field strengths of the $SU(2)_0$, $SU(2)_1$ and $U(1)_2$ gauge symmetries, respectively. According to our assignments for Φ_1 and Φ_2 , we can write down the general Higgs potential $V(\Phi_1, \Phi_2)$ under the 221 gauge group \mathcal{G} ,

$$\begin{aligned} V(\Phi_1, \Phi_2) = & \frac{1}{2} \lambda_1 \left[\text{tr}(\Phi_1^\dagger \Phi_1) - \frac{f_1^2}{2} \right]^2 + \frac{1}{2} \lambda_2 \left[\text{tr}(\Phi_2^\dagger \Phi_2) - \frac{f_2^2}{2} \right]^2 \\ & + \lambda_{12} \left[\text{tr}(\Phi_1^\dagger \Phi_1) - \frac{f_1^2}{2} \right] \left[\text{tr}(\Phi_2^\dagger \Phi_2) - \frac{f_2^2}{2} \right]. \end{aligned} \quad (2.3)$$

Unlike the 3-site model [9], we construct Φ_1 and Φ_2 in the linear realization with physical Higgs bosons. Hence, our 221 model is renormalizable and provides an effective UV completion of the 3-site model. Here we use the matrix representation for the Higgs fields,

$$\Phi_j = \frac{1}{2} (f_j + h_j + i\tau^a \pi_j^a), \quad (2.4)$$

with the Pauli matrices τ^a and two Higgs VEVs $f_j \in (f_1, f_2)$. In this representation, the covariant derivatives of Φ_j are given by

$$D_\mu \Phi_1 = \partial_\mu \Phi_1 + ig_0 \frac{\tau^a}{2} W_{0\mu}^a \Phi_1 - ig_1 \Phi_1 \frac{\tau^a}{2} W_{1\mu}^a, \quad (2.5a)$$

$$D_\mu \Phi_2 = \partial_\mu \Phi_2 + ig_1 \frac{\tau^a}{2} W_{1\mu}^a \Phi_2 - ig_2 \Phi_2 \frac{\tau^3}{2} B_{2\mu}. \quad (2.5b)$$

Besides of the SM gauge boson (W, Z, γ), there are three new gauge bosons (W', Z') in the gauge sector. Under the gauge symmetry breaking (2.1), all massive gauge bosons acquire their masses as follows,

$$m_W^2 = \frac{1}{4} \frac{g_0^2 f_2^2}{1+r^2} \left[1 - \frac{x^2}{(1+r^2)^2} + \mathcal{O}(x^4) \right], \quad (2.6a)$$

$$m_Z^2 = \frac{1}{4c^2} \frac{g_0^2 f_2^2}{1+r^2} \left[1 - \frac{(c^2 - r^2 s^2)^2 x^2}{c^2 (1+r^2)^2} + \mathcal{O}(x^4) \right], \quad (2.6b)$$

$$M_{W'}^2 = \frac{1}{4} g_1^2 f_1^2 (1+r^2) \left[1 + \frac{x^2}{(1+r^2)^2} + \mathcal{O}(x^4) \right], \quad (2.6c)$$

$$M_{Z'}^2 = \frac{1}{4} g_1^2 f_1^2 (1+r^2) \left[1 + \frac{1+r^4 (s^2/c^2)}{(1+r^2)^2} x^2 + \mathcal{O}(x^4) \right], \quad (2.6d)$$

where $x^2 \equiv g_0^2/g_1^2 \ll 1$ is a small parameter under $g_1^2 \gg g_0^2, g_2^2$, and $r \equiv f_2/f_1$ is the VEV ratio. In (2.6b) and (2.6d), we have adopted the notation, $(c, s) \equiv (\cos \theta, \sin \theta)$, with $s/c \equiv g_2/g_0$. From (2.6a) and (2.6c), we can reexpress the small expansion parameter x as,

$$x = \frac{1+r^2}{r} \frac{m_W}{M_{W'}} \left[1 + \frac{m_W^2}{r^2 M_{W'}^2} + \mathcal{O}\left(\frac{m_W^4}{M_{W'}^4}\right) \right]. \quad (2.7)$$

The formulae given in this subsection hold for general VEVs (f_1, f_2) , which extend the gauge-sector results of the 3-site model under $f_1 = f_2$ [9]. We note that the W' and Z' are nearly degenerate and their masses differ only at the $\mathcal{O}(x^2)$. The two Higgs VEVs (f_1, f_2) are connected to the Fermi constant G_F via

$$\frac{1}{f_1^2} + \frac{1}{f_2^2} = \frac{1}{v^2}, \quad (2.8)$$

where

$$v^2 = v_0^2 \left[1 - \frac{2r^2}{(1+r^2)^2} x^2 + \frac{(3+r^2)r^2}{(1+r^2)^4} x^4 + \mathcal{O}(x^6) \right], \quad (2.9)$$

and $v_0^2 \equiv (\sqrt{2}G_F)^{-1}$ [9]. Thus, we have $f_2 = v\sqrt{1+r^2}$. So, from the formulae (2.6a)-(2.6b), it is clear that under $g_1^2 \gg g_0^2, g_2^2$, we can approximately identify g_0 and g_2 as the SM electroweak gauge couplings. It can be further shown that the angle $\theta = \arctan(g_2/g_0)$ approximates the Weinberg angle θ_W of the SM up to $\mathcal{O}(x^2)$ corrections. In addition, the mass-eigenstates are related to the gauge eigenstates as follows,

$$W_\mu \simeq W_{0\mu}^\pm + \frac{x}{1+r^2} W_{1\mu}^\pm, \quad (2.10a)$$

$$W'_\mu \simeq W_{1\mu}^\pm - \frac{x}{1+r^2} W_{0\mu}^\pm, \quad (2.10b)$$

$$Z_\mu \simeq (cW_{0\mu}^3 - sB_{2\mu}) + x \frac{c^2 - s^2 r^2}{c(1+r^2)} W_{1\mu}^3, \quad (2.10c)$$

$$Z'_\mu \simeq W_{1\mu}^3 - \frac{x}{1+r^2} W_{0\mu}^3 - x \frac{s r^2}{1+r^2} B_{2\mu}, \quad (2.10d)$$

with $\mathcal{O}(x^3)$ corrections neglected. The massless photon field is exactly expressed as,

$$A_\mu = \frac{e}{g_0} W_{0\mu}^3 + \frac{e}{g_1} W_{1\mu}^3 + \frac{e}{g_2} B_{2\mu}, \quad (2.11)$$

where the QED gauge coupling e of the unbroken $U(1)_{\text{em}}$ is inferred from the gauge couplings of the group \mathcal{G} ,

$$\frac{1}{e^2} = \frac{1}{g_0^2} + \frac{1}{g_1^2} + \frac{1}{g_2^2}. \quad (2.12)$$

From the expressions (2.10a)-(2.10d), we see that $W_{0\mu}^a$ and $B_{2\mu}$ are approximately the gauge bosons of the SM gauge group $SU(2)_L \times U(1)_Y$, while $W_{1\mu}^a$ are mainly the new gauge bosons

$W'_\mu{}^a$. Due to the mixing between the lighter and heavier gauge bosons, the WWZ coupling becomes different from the SM value. The LEP-II limit on this coupling translates into a lower bound on the W' mass, around 300 GeV [9, 10].

2.2 Higgs Sector of the Model

Minimizing the Higgs potential (2.3), we find that $\langle \Phi_1 \rangle = \frac{1}{2}f_1 \mathbb{I}_{2 \times 2}$ and $\langle \Phi_2 \rangle = \frac{1}{2}f_2 \mathbb{I}_{2 \times 2}$, under the following conditions,

$$\lambda_1, \lambda_2 > 0, \quad \lambda_1 \lambda_2 \neq \lambda_{12}^2. \quad (2.13)$$

After spontaneous symmetry breaking, six would-be Nambu-Goldstones (π_1^a, π_2^a) are eaten by the gauge bosons (W_1^a, W_2^a) which compose the longitudinal components of the lighter mass-eigenstates (W, Z) and the heavier ones (W', Z'). Only two physical CP-even neutral scalars (h_1, h_2) survive. This is very different from the conventional two-Higgs-doublet model which contains five physical Higgs states. The mass matrix for the CP-even states (h_1, h_2) can be generally expressed as,

$$-\frac{1}{2} \begin{pmatrix} h_1 & h_2 \end{pmatrix} \begin{pmatrix} \lambda_1 f_1^2 & \lambda_{12} f_1 f_2 \\ \lambda_{12} f_1 f_2 & \lambda_2 f_2^2 \end{pmatrix} \begin{pmatrix} h_1 \\ h_2 \end{pmatrix}, \quad (2.14)$$

which is diagonalized by the orthogonal transformation,

$$\begin{pmatrix} c_\alpha & -s_\alpha \\ s_\alpha & c_\alpha \end{pmatrix} \begin{pmatrix} \lambda_1 f_1^2 & \lambda_{12} f_1 f_2 \\ \lambda_{12} f_1 f_2 & \lambda_2 f_2^2 \end{pmatrix} \begin{pmatrix} c_\alpha & s_\alpha \\ -s_\alpha & c_\alpha \end{pmatrix} = \begin{pmatrix} M_h^2 & 0 \\ 0 & M_H^2 \end{pmatrix}, \quad (2.15)$$

where mass-eigenstates (h, H) are connected to the gauge-eigenstates (h_1, h_2) via

$$\begin{pmatrix} h \\ H \end{pmatrix} = \begin{pmatrix} c_\alpha & -s_\alpha \\ s_\alpha & c_\alpha \end{pmatrix} \begin{pmatrix} h_1 \\ h_2 \end{pmatrix}. \quad (2.16)$$

Thus we can derive the mass-eigenvalues $M_{h,H}^2$ and the mixing angle α ,

$$M_{h,H}^2 = \frac{1}{2} \left[(\lambda_1 f_1^2 + \lambda_2 f_2^2) \mp \sqrt{(\lambda_1 f_1^2 - \lambda_2 f_2^2)^2 + 4\lambda_{12}^2 f_1^2 f_2^2} \right], \quad (2.17a)$$

$$\sin 2\alpha = \frac{2\lambda_{12}}{\sqrt{(\lambda_1 r^{-1} - \lambda_2 r)^2 + 4\lambda_{12}^2}}, \quad (2.17b)$$

where $r = f_2/f_1$ is the VEV ratio introduced earlier. In (2.17a), the positivity condition of the lighter Higgs mass $M_h^2 > 0$ further requires,

$$\lambda_1 \lambda_2 > \lambda_{12}^2. \quad (2.18)$$

which also holds the second inequality of (2.13). We note that the conditions (2.13) and (2.18) ensure the tree-level vacuum stability of the Higgs potential.

Finally, inspecting Eq. (2.3) we see that the Higgs potential contains five parameters in all, namely, $(\lambda_1, \lambda_2, \lambda_{12})$ and (f_1, f_2) . Imposing the new LHC data of $M_h \simeq 125 \text{ GeV}$ [3, 4] and the VEV condition (2.8) with the Fermi constant G_F , we are left with three input parameters of (M_H, α, r) . Here the VEV ratio $r = 1$ is the default of the 3-site model [9] for collective symmetry breaking. In the current study, we also set $r = 1$ as our default, but we will further explore wider parameter space with $r = \mathcal{O}(1)$. Hence, from the VEV condition (2.8) with G_F , and given the ratio r and the lighter Higgs mass $M_h \simeq 125 \text{ GeV}$ [3, 4], we only have two free parameters in the Higgs sector, which can be expressed as the Higgs mixing angle α and the heavier Higgs mass M_H . In the gauge sector, the three gauge couplings (g_0, g_1, g_2) can be fixed by inputting the fine-structure constant $\alpha_{\text{em}} = e^2/4\pi$ via (2.12) together with the gauge boson masses (m_W, M'_W) via (2.6), i.e., $(\alpha_{\text{em}}, m_W, M'_W)$, or equivalently, $(\alpha_{\text{em}}, m_Z, M'_W)$.

In the following sections, we will perform the LHC analyses based on the two major input parameters (α, M_H) . The other secondary input parameters include the VEV ratio $r = \mathcal{O}(1)$, the heavier gauge boson mass $M'_W \gtrsim 300 \text{ GeV}$, and the heavier fermion mass $M_F \gtrsim 1.8 \text{ TeV}$, as will be summarized in Eq. (2.23). We will first identify the proper parameter range of the Higgs mixing angle α which gives rise to the observed $\gamma\gamma$ signals of the light Higgs boson h around 125 GeV. Then, we further predict the signals for the heavier Higgs boson H via WW and ZZ channels over the wide mass-ranges of $M_H = 130 - 600 \text{ GeV}$, as a new physics discriminator from the SM.

2.3 Fermion Sector of the Model

The fermion sector contains the left-handed Weyl fermions Ψ_{0L} , the right-handed Weyl fermions $\Psi_{2R} = (\Psi_{2R}^u, \Psi_{2R}^d)$, and the vector-like fermions $\Psi_1 = (\Psi_{1L}, \Psi_{1R})$. Same as the 3-site model [9], these vector-like fermions Ψ_1 are necessary for the ideal delocalization condition and providing compatible results for the precision electroweak measurement [14]. In addition, the vector-like fermions Ψ_1 can naturally have gauge-invariant renormalizable mass-term. The representations for fermions are summarized in Table 1.

With these, we can write down the Higgs Yukawa interactions and fermion mass-terms in this model,

$$\mathcal{L}_Y = - \sum_{i,j} \left[y_{1ij} \bar{\Psi}_{0L}^i \Phi_1 \Psi_{1R}^j + \bar{\Psi}_{1L}^i \Phi_2 y_{2ij} \Psi_{2R}^j + \bar{\Psi}_{1L}^i M_{ij} \Psi_{1R}^j + \text{h.c.} \right], \quad (2.19)$$

where $i, j = 1, 2, 3$ are the generational indices. M_{ij} represents a Dirac mass matrix, and $y_{2ij} = \text{diag}(y_2^u, y_2^d)_{ij}$. In general, y_{1ij} and M_{ij} are not flavor-blind. For consistency with the FCNC constraints on the off-diagonal components of y_{1ij} and M_{ij} [21], we will set y_{1ij} and M_{ij} to be flavor-diagonal, i.e., $y_{1ij} = y_1 \delta_{ij}$ and $M_{ij} = M_F \delta_{ij}$. With this, all flavor structures in this model are embedded in y_{2u} and y_{2d} . We also consider $M_F \gg y_1 f_1$ and $M_F \gg (y_2^u, y_2^d) f_2$. This makes the non-SM fermion masses much heavier than the SM fermion masses, and makes Ψ_{0L} and Ψ_{2R} approximately behave like the SM fermions. It is

Table 1. Assignments for fermions under the gauge group of the present model. In the fourth and fifth columns, the $U(1)_2$ charges and $SU(3)_c$ representations are shown for the quarks (without parentheses) and leptons (in parentheses), respectively.

Fermions	$SU(2)_0$	$SU(2)_1$	$U(1)_2$	$SU(3)_c$
Ψ_{0L}	2	1	$\frac{1}{6} (-\frac{1}{2})$	3 (1)
Ψ_{1L}	1	2	$\frac{1}{6} (-\frac{1}{2})$	3 (1)
Ψ_{1R}	1	2	$\frac{1}{6} (-\frac{1}{2})$	3 (1)
Ψ_{2R}^u	1	1	$\frac{2}{3} (0)$	3 (1)
Ψ_{2R}^d	1	1	$-\frac{1}{3} (-1)$	3 (1)

also consistent with the fact $SU(2)_0 \times U(1)_2 \approx SU(2)_L \times U(1)_Y$, as we commented earlier. For simplicity, we will take the same M_F and y_1 values in both quark and lepton sectors for the present study. The mass-eigenstates for the quark sector are expressed as, up to $\mathcal{O}(\epsilon_L^2, \epsilon_R^2)$ corrections,

$$q_L \simeq -\Psi_{0L} + \epsilon_L \Psi_{1L}, \quad q_R \simeq -\epsilon_R \Psi_{1R} + \Psi_{2R}, \quad (2.20a)$$

$$Q_L \simeq -\epsilon_L \Psi_{0L} - \Psi_{1L}, \quad Q_R \simeq \Psi_{1R} + \epsilon_R \Psi_{2R}, \quad (2.20b)$$

where $q_{L,R}$ denote the SM quarks, and $Q_{L,R}$ represent the corresponding heavy fermions. The relations for lepton sector are expressed in a similar manner. Eq. (2.20) contains two small parameters, $\epsilon_L = y_1 f_1 / (2M_F) \ll 1$, and $\epsilon_R = y_2 f_2 / (2M_F) \ll 1$. It is clear that Ψ_{L0} and Ψ_{R2} are approximately the SM fermions. Up to $\mathcal{O}(\epsilon_L^2)$ and $\mathcal{O}(\epsilon_R^2)$ corrections, the mass-eigenvalues for the SM fermions and the heavy fermions are given by,

$$m_q \simeq \epsilon_L \epsilon_R M_F, \quad M_Q \simeq M_F. \quad (2.21)$$

The light fermion mass-term is proportional to ϵ_R , or y_2 , which has all flavor structures and mass hierarchies embedded.

The couplings between the SM gauge boson and the SM fermions, such as $g_{Zf_L f_L}$, are different from those in the SM due to the mixing among the SM particles and extra heavy particles. This leads to nonzero electroweak parameter S [22] at the tree-level. Such contributions to the S parameter can be reduced to zero by adjusting ϵ_L as follows [9],

$$\epsilon_L = \frac{m_W}{M_{W'}} (1 + r^{-2})^{\frac{1}{2}} [1 + \mathcal{O}(x^2)], \quad (2.22)$$

via the ideal delocalization [14]³, where $r \equiv f_2/f_1$. To keep ϵ_L small, it is necessary to control the ratio f_2/f_1 . For the phenomenological analyses, we will take the natural parameter range,

³It is also possible to make S small enough by considering large W' mass of $\mathcal{O}(1)$ TeV or above. We do not pursue this possibility for the current construction.

$\frac{1}{2} \lesssim f_2/f_1 \lesssim 2$. The heavy fermion mass-parameter M_F is constrained by the T parameter, which gives a lower limit, $M_F > 1.8 \text{ TeV}$ [9, 21].

As a summary of the model setup, we list the parameter sets and the relevant ranges consistent with the low energy precision constraints,

$$\begin{aligned} \frac{1}{2} &\lesssim f_2/f_1 \lesssim 2, & \alpha &\in [0, \pi), \\ M_F &\gtrsim 1.8 \text{ TeV}, & M_{W'} &\gtrsim 300 \text{ GeV}. \end{aligned} \quad (2.23)$$

As we will demonstrate in the next two sections, the predictions of Higgs signal are mostly sensitive to the mixing angle α . The other model parameters varying within the ranges of (2.23) only yield sub-leading contributions.

2.4 Couplings of Higgs Bosons, Gauge Bosons and Fermions

In this subsection, we present the Higgs boson couplings with gauge bosons and fermions, as well as the gauge boson couplings with fermions. These will be needed for our analyses of Higgs productions and decays in the next two sections.

2.4.1 Gauge and Yukawa Couplings of Higgs Bosons

We analyze the gauge and Yukawa couplings of the CP-even Higgs bosons h^0 and H^0 , respectively. For the light weak gauge bosons $V (= W, Z)$, the triple Higgs-gauge couplings G_{hVV} and G_{HVV} take the following forms up to $\mathcal{O}(x^2)$ corrections,

$$G_{hVV} = G_{hVV}^{\text{SM}} \xi_{hVV}, \quad G_{HVV} = G_{hVV}^{\text{SM}} \xi_{HVV}, \quad (2.24a)$$

$$\xi_{hWW} = \frac{r^3 c_\alpha - s_\alpha}{(1+r^2)^{3/2}} + \frac{r^2[-3s_\alpha + (r^3 - 2r)c_\alpha]}{(1+r^2)^{7/2}} x^2, \quad (2.24b)$$

$$\xi_{hZZ} = \frac{r^3 c_\alpha - s_\alpha}{(1+r^2)^{3/2}} + \frac{r^2[(-3 + s_W^2(3+2r))s_\alpha + ((r^3 - 2r) + s_W^2 r(r^2 + 2))c_\alpha]}{c_W^2 (1+r^2)^{7/2}} x^2, \quad (2.24c)$$

$$\xi_{HWW} = \frac{r^3 s_\alpha + c_\alpha}{(1+r^2)^{3/2}} + \frac{r^2[3c_\alpha + (r^3 - 2r)s_\alpha]}{(1+r^2)^{7/2}} x^2, \quad (2.24d)$$

$$\xi_{HZZ} = \frac{r^3 s_\alpha + c_\alpha}{(1+r^2)^{3/2}} + \frac{r^2[(3 - s_W^2(3+2r))c_\alpha + ((r^3 - 2r) + s_W^2 r(r^2 + 2))s_\alpha]}{c_W^2 (1+r^2)^{7/2}} x^2, \quad (2.24e)$$

with $G_{hVV}^{\text{SM}} = 2M_V^2/v_0$ for $V = W, Z$.

An important feature of the Higgs-gauge-boson triple coupling G_{hVV} is that it vanishes when the Higgs mixing angle α takes a special value, $\tan \alpha \simeq r^3$, where $r \equiv f_2/f_1$. In this case, the light Higgs boson h becomes gaugephobic regarding its triple couplings. The corresponding collider phenomenology of h^0 would deviate from the SM Higgs boson substantially. Similarly, for the special mixing angle $\tan \alpha \simeq -1/r^3$, the G_{HVV} coupling vanishes, and thus

H Higgs state becomes gaugephobic so long as the triple coupling is concerned. We note that with the generic choices of two Higgs VEVs, $r = f_2/f_1 \sim \mathcal{O}(1)$, G_{hVV} and G_{HVV} couplings are always smaller than G_{hVV}^{SM} for any mixing angle α .

The Yukawa couplings between the Higgs bosons and the SM fermions are also modified relative to the SM values. We derive these couplings in following form up to $\mathcal{O}(\epsilon_L^2)$ and $\mathcal{O}(\epsilon_R^2)$ corrections,

$$G_{hff} = \frac{m_f}{v_0} \xi_{hff}, \quad G_{Hff} = \frac{m_f}{v_0} \xi_{Hff}, \quad (2.25a)$$

$$\xi_{hff} = \frac{rc_\alpha - s_\alpha}{\sqrt{1+r^2}} - \frac{r(rs_\alpha + c_\alpha)}{(1+r^2)^{5/2}} x^2 + \frac{s_\alpha \sqrt{1+r^2}}{x^2} \frac{m_f^2}{M_F^2}, \quad (2.25b)$$

$$\xi_{Hff} = \frac{rs_\alpha + c_\alpha}{\sqrt{1+r^2}} - \frac{r(-rc_\alpha + s_\alpha)}{(1+r^2)^{5/2}} x^2 - \frac{c_\alpha \sqrt{1+r^2}}{x^2} \frac{m_f^2}{M_F^2}, \quad (2.25c)$$

We see that the Yukawa couplings for both h^0 and H^0 are always smaller than the corresponding SM Yukawa couplings, i.e., $|\xi_{hff}| \leq 1$ and $|\xi_{Hff}| \leq 1$. Moreover, the Yukawa couplings ξ_{hff} or ξ_{Hff} vanishes under the special value of mixing angle $\tan \alpha = r$ or $\tan \alpha = -1/r$, and thus h or H becomes fermiophobic.

We also analyze the additional Higgs couplings with the new gauge bosons V' ($= W', Z'$) and new fermions F . The new particles V' and F will appear in the loop-induced Higgs boson productions and decays. At the leading order, we derive these additional new couplings of the Higgs boson h^0 as follows,

$$G_{hVV'} = \frac{2m_V M_{V'}}{v_0} \xi_{hVV'}, \quad \xi_{hVV'} = -\frac{r(s_\alpha + rc_\alpha)}{(1+r^2)^{3/2}}, \quad (2.26a)$$

$$G_{hV'V'} = \frac{2M_{V'}^2}{v_0} \xi_{hV'V'}, \quad \xi_{hV'V'} = \frac{r(c_\alpha - rs_\alpha)}{(1+r^2)^{3/2}}, \quad (2.26b)$$

$$G_{h\bar{f}_L F_R} = \frac{M_F}{v_0} \xi_{h\bar{f}_L F_R}, \quad \xi_{h\bar{f}_L F_R} = \frac{c_\alpha r}{1+r^2} x, \quad (2.26c)$$

$$G_{h\bar{F}_L f_R} = \frac{m_f}{v_0} \xi_{h\bar{F}_L f_R}, \quad \xi_{h\bar{F}_L f_R} = \frac{s_\alpha}{x}, \quad (2.26d)$$

$$G_{h\bar{F}_L F_R} = \frac{M_F}{v_0} \xi_{h\bar{F}_L F_R}, \quad \xi_{h\bar{F}_L F_R} = \frac{c_\alpha r x^2}{(1+r^2)^{3/2}} - \frac{s_\alpha \sqrt{1+r^2}}{x^2} \frac{m_f^2}{M_F^2}, \quad (2.26e)$$

where M_F denote the heavy fermion masses. Due to the ideal delocalization result (2.22), the Higgs couplings to the new heavy fermions depend on the gauge boson masses. These couplings enter the loop-induced processes for the Higgs boson productions and decays, and their effects will be taken into account in the following numerical analysis.

In parallel, we derive couplings of the heavier Higgs boson H^0 with new gauge bosons V' and new fermions F , which are obtained by making the replacement of $(c_\alpha, s_\alpha) \rightarrow (s_\alpha, -c_\alpha)$,

$$G_{HVV'} = \frac{2m_V M_{V'}}{v_0} \xi_{HVV'}, \quad \xi_{HVV'} = -\frac{r(rs_\alpha - c_\alpha)}{(1+r^2)^{3/2}}, \quad (2.27a)$$

$$G_{HV'V'} = \frac{2M_{V'}^2}{v_0} \xi_{HV'V'}, \quad \xi_{HV'V'} = \frac{r(s_\alpha + rc_\alpha)}{(1+r^2)^{3/2}}, \quad (2.27b)$$

$$G_{H\bar{f}_L F_R} = \frac{M_F}{v_0} \xi_{H\bar{f}_L F_R}, \quad \xi_{H\bar{f}_L F_R} = \frac{s_\alpha r}{1+r^2} x, \quad (2.27c)$$

$$G_{H\bar{F}_L f_R} = \frac{m_f}{v_0} \xi_{H\bar{F}_L f_R}, \quad \xi_{H\bar{F}_L f_R} = -\frac{c_\alpha}{x}, \quad (2.27d)$$

$$G_{H\bar{F}_L F_R} = \frac{M_F}{v_0} \xi_{HFF}, \quad \xi_{HFF} = \frac{s_\alpha r x^2}{(1+r^2)^{3/2}} + \frac{c_\alpha \sqrt{1+r^2}}{x^2} \frac{m_f^2}{M_F^2}. \quad (2.27e)$$

2.4.2 Gauge Boson Self-Couplings and Gauge-Fermion Couplings

Besides the above gauge and Yukawa couplings with Higgs bosons, some of the gauge boson self-couplings and gauge-fermion couplings invoke both the SM fields and the extra heavy states. They will contribute to the unitarity sum rules (Sec. 2.5) and the loop-induced Higgs decay channels (Appendix).

We first summarize the cubic gauge couplings of VVV' and $VV'V'$ with extra V' ($= W', Z'$) gauge bosons up to the $\mathcal{O}(x^2)$ corrections,

$$G_{WW\gamma} = G_{W'W'\gamma} = e, \quad G_{WW'\gamma} = 0, \quad (2.28a)$$

$$G_{WWZ'} = -\frac{e}{s_W} \frac{r^2 x}{(1+r^2)^2}, \quad G_{WW'Z} = \frac{e}{s_W c_W} \frac{r^2 x}{(1+r^2)^2}, \quad (2.28b)$$

$$G_{WW'Z'} = \frac{e}{s_W} \frac{1}{1+r^2}, \quad G_{W'W'Z} = \frac{e}{s_W c_W} \frac{c_W^2 - s_W^2 r^2}{1+r^2}. \quad (2.28c)$$

For quartic gauge couplings, we include both $VVVV$ couplings and those involving the $\gamma\gamma$ or $Z\gamma$, as relevant to our phenomenological analysis,

$$G_{WWWW} = \frac{e^2}{s_W^2} \left[1 - \frac{1-2r^2}{(1+r^2)^2} x^2 \right], \quad G_{WWZZ} = \frac{e^2}{s_W^2} \left[c_W^2 - \frac{c_W^2 - 2r^2}{(1+r^2)^2} x^2 \right], \quad (2.29a)$$

$$G_{WW\gamma\gamma} = G_{W'W'\gamma\gamma} = e^2, \quad G_{WW'\gamma\gamma} = 0, \quad (2.29b)$$

$$G_{WWZ\gamma} = eG_{WWZ}, \quad G_{WW'Z\gamma} = eG_{WW'Z}, \quad G_{W'W'Z\gamma} = eG_{W'W'Z}. \quad (2.29c)$$

Finally, we derive all relevant couplings of the light weak gauge bosons W or Z with the fermions. For the W couplings to the fermion pairs, we have,

$$G_{W\bar{f}'_L f_L} = \frac{e}{s_W}, \quad (2.30a)$$

$$G_{W\bar{F}_L f_L} = G_{W\bar{f}_L F_L} = \frac{e}{s_W} \frac{r^2}{(1+r^2)^{3/2}} x, \quad (2.30b)$$

$$G_{W\bar{F}_L F_L} = \frac{e}{s_W} \frac{1}{1+r^2}, \quad (2.30c)$$

$$G_{W\bar{f}_R f_R} = \frac{e}{s_W} \frac{m_u m_d}{M_F^2} \frac{1}{x^2}, \quad (2.30d)$$

$$G_{W\bar{U}_R d_R} = \frac{e}{s_W} \frac{1}{(1+r^2)^{1/2}} \frac{m_d}{M_F} \frac{1}{x}, \quad (2.30e)$$

$$G_{W\bar{u}_R D_R} = \frac{e}{s_W} \frac{1}{(1+r^2)^{1/2}} \frac{m_u}{M_F} \frac{1}{x}, \quad (2.30f)$$

$$G_{W\bar{F}_R F_R} = \frac{e}{s_W} \frac{1}{1+r^2}. \quad (2.30g)$$

Then, we present the fermion couplings with weak gauge boson Z , which are also relevant for the decay analysis of $h^0 \rightarrow Z\gamma$,

$$G_{Z\bar{f}_L f_L} = \frac{e}{s_W c_W} (T_{3f} - Q_f s_W^2), \quad (2.31a)$$

$$G_{Z\bar{f}_R f_R} = \frac{e}{s_W c_W} \left(\frac{T_{3f}}{x^2} \frac{m_f^2}{M_F^2} - Q_f s_W^2 \right), \quad (2.31b)$$

$$G_{Z\bar{F}_L F_L} = G_{Z\bar{F}_R F_R} = \frac{e}{s_W c_W} \left(\frac{T_{3f}}{1+r^2} - Q_f s_W^2 \right), \quad (2.31c)$$

$$G_{Z\bar{F}_L f_L} = G_{Z\bar{f}_L F_L} = \frac{e}{s_W c_W} \frac{T_{3f} r^2 x}{(1+r^2)^{3/2}}, \quad (2.31d)$$

$$G_{Z\bar{F}_R f_R} = G_{Z\bar{f}_R F_R} = \frac{e}{s_W c_W} \frac{T_{3f} r}{(1+r^2)^{1/2}} \frac{m_f}{M_F}, \quad (2.31e)$$

where $T_{3f} = \pm\frac{1}{2}$ are isospins for the up-type and down-type fermions, respectively.

2.5 Unitarity: Roles of Spin-1 Gauge Bosons versus Spin-0 Higgs Bosons

In the conventional SM, a single physical Higgs boson plays the key role to ensure exact E^2 cancellation in the amplitudes of longitudinal weak boson scattering $V_L V_L \rightarrow V_L V_L$ at high energies [23]. The present 221 model has two spin-0 neutral Higgs bosons (h^0, H^0) and three new spin-1 gauge bosons (W', Z'), which will cooperate together to ensure the exact E^2 cancellation in the $V_L V_L$ scattering, so long as the masses of h^0/H^0 and W'/Z' are below about 1 TeV. Hence, it differs from either the conventional SM, or the 5d Higgsless models [24] in which the extra longitudinal Kaluza-Klein (KK) gauge bosons alone ensure the E^2 cancellation [25].⁴ We will show that even for the special parameter choice of $\tan\alpha = r^3$ (which corresponds to vanishing hVV coupling and thus a gaugephobic Higgs boson h^0), the perturbative unitarity is preserved by the heavier Higgs boson H^0 together with W'/Z' . This conceptually differs from the conventional two-Higgs-doublet models under the SM gauge group as there is no extra gauge bosons W'/Z' to participate in the E^2 cancellation and

⁴It also differs from the recent unitarization proposal [26] via spontaneous dimensional reduction (SDR), where the $V_L V_L$ scattering cross sections get unitarized through the reduced phase-space under SDR at high energies.

unitarity; it also differs from all other extra SU(2) models in the literature [17–20] with a large splitting between the two Higgs VEVs which make the W'/Z' masses significantly above 1 TeV and thus irrelevant to the unitarization of $V_L V_L$ scattering.

We analyze the perturbative unitarity of the 221 model in this subsection. For the purpose of unitarity analysis, it is sufficient to set the $U(1)_2$ gauge coupling $g_2 = 0$, so there is no photon-related mixings. We perform a unitary gauge computation of the $V_L V_L \rightarrow V_L V_L$ amplitude in the present model. Requiring the E^2 cancellation, we derive the following sum rule on the quartic couplings (G_{VVVV}) and triple couplings (G_{VVV} , $G_{V'VV}$, G_{hVV} , G_{HVV}),

$$G_{VVVV} - \frac{3}{4}G_{VVV}^2 = \frac{3}{4} \frac{M_{V'}^2}{m_V^2} G_{V'VV}^2 + \frac{G_{hVV}^2 + G_{HVV}^2}{4m_V^2}, \quad (2.32)$$

where $V = W, Z$. This sum rule can be readily extended to more general cases with multiple new gauge bosons $V_n (= V', V'', V''', \dots)$ and multiple Higgs bosons $H_n (= h, H, H', H'', \dots)$. Thus, the two terms on the right-hand side (RHS) of (2.32) will be replaced by the sums over V_n and H_n in general,

$$G_{VVVV} - \frac{3}{4}G_{VVV}^2 = \sum_n \frac{3}{4} \frac{M_{V_n}^2}{m_V^2} G_{VVV_n}^2 + \sum_n \frac{G_{VVH_n}^2}{4m_V^2}. \quad (2.33)$$

Let us inspect the sum rule (2.32) further. The left-hand side (LHS) of (2.32) is the coefficient of the non-canceled E^2 terms of the V_L -amplitude from the pure Yang-Mills gauge-interactions involving only the light gauge bosons W/Z ; while the first term on the RHS of (2.32) is the coefficient of the contributions given by the V' -exchanges ($V' = W', Z'$), and the second term on the RHS comes from the (h, H) Higgs-exchanges. The net coefficient of the E^2 term equals the difference between the two sides of (2.32). Hence, the exact E^2 cancellation is ensured by holding the sum rule (2.32). It is now evident that *the 221 model achieves the exact E^2 cancellation by the joint role of exchanging both spin-1 new gauge bosons and spin-0 Higgs bosons*. Hence, this joint unitarization mechanism differs from either the conventional unitarization of the SM (with Higgs-exchange alone) or the 5d Higgsless unitarization (with exchanges of W'/Z' -like gauge KK-modes alone).

We have explicitly verified the validity of (2.32) in this model. Due to the Higgs boson mass-diagonalization and rotation in (2.16)-(2.17), we note that the Higgs mass-eigenstate couplings G_{hVV} and G_{HVV} in (2.32) are connected to their corresponding weak-eigenstate couplings G_{h_1VV} and G_{h_2VV} ,

$$G_{hVV} = c_\alpha G_{h_1VV} - s_\alpha G_{h_2VV}, \quad (2.34a)$$

$$G_{HVV} = s_\alpha G_{h_1VV} + c_\alpha G_{h_2VV}, \quad (2.34b)$$

where the weak-eigenstate couplings G_{h_1VV} and G_{h_2VV} are independent of the Higgs mixing angle α . From (2.34), we readily deduce the sum of two squared Higgs couplings in the last term of (2.32),

$$G_{hVV}^2 + G_{HVV}^2 = G_{h_1VV}^2 + G_{h_2VV}^2, \quad (2.35)$$

which does not depend on the mixing angle α . From the hVV and HVV couplings in (2.24), we can explicitly compute the sum,

$$\frac{G_{hVV}^2 + G_{HVV}^2}{(G_{hVV}^{\text{SM}})^2} = \xi_{hVV}^2 + \xi_{HVV}^2 = \frac{1+r^6}{(1+r^2)^3} + \frac{2r^2(r^4-3r^2+3)}{(1+r^2)^4}x^2 + \mathcal{O}(x^4), \quad (2.36)$$

which invokes only the VEV ratio $r = f_2/f_1$ and the gauge coupling ratio $x = g_0/g_1$. This means that for h^0 in the gaugephobic limit $\xi_{hVV} = 0$ (under $\tan\alpha = r^3$), the role of the Higgs-exchange in the unitarity sum rule (2.32) is played by the heavier Higgs boson H^0 alone. Vice versa, for H^0 in gaugephobic limit of $\xi_{HVV} = 0$ (under $\tan\alpha = -1/r^3$), it is the lighter Higgs boson h^0 that plays the full role of the Higgs-exchange in the unitarity sum rule (2.32).

For illustration, we explicitly analyze two longitudinal weak boson scattering processes, namely, $W_L W_L \rightarrow \frac{1}{\sqrt{2}}Z_L Z_L$ and $W_L Z_L \rightarrow W_L Z_L$. The scattering amplitudes of these two processes include the following types of contributions,

$$\mathcal{M}(W_L W_L \rightarrow \frac{1}{\sqrt{2}}Z_L Z_L) = \mathcal{M}_{\text{ct}} + \mathcal{M}_{W/W'}^{(t)} + \mathcal{M}_{W/W'}^{(u)} + \mathcal{M}_{h/H}^{(s)}, \quad (2.37a)$$

$$\mathcal{M}(W_L Z_L \rightarrow W_L Z_L) = \mathcal{M}_{\text{ct}} + \mathcal{M}_{W/W'}^{(s)} + \mathcal{M}_{W/W'}^{(t)} + \mathcal{M}_{h/H}^{(t)}, \quad (2.37b)$$

where \mathcal{M}_{ct} denotes the contact interaction amplitude, and $\mathcal{M}_X^{(j)}$ stands for the exchange of particle X via j -channel ($j = s, t, u$). In the above, the W' -exchange enters the t/u -channel (s/t -channel) of the first (second) process and the (h, H) -exchanges appear in the s -channel (t -channel) of the first (second) process. The corresponding s -wave amplitudes are computed from,

$$a_0(s) = \frac{1}{32\pi} \int_{-1}^1 d(\cos\theta) \mathcal{M}(s, \theta), \quad (2.38)$$

where \sqrt{s} is the scattering energy in the center-of-mass frame and θ is the scattering angle.

In Fig. 1, we plot the s -wave amplitude $a_0(W_L W_L \rightarrow \frac{1}{\sqrt{2}}Z_L Z_L)$ as a function of scattering energy \sqrt{s} . In plot-(a), we separately display the individual contributions from the pure Yang-Mills (YM) in purple curve (including contact terms plus the W -exchange contribution), the W' -exchange (blue curve), the h/H -exchanges (green curve), and the total sum of all three types of contributions (red curve, marked by YM+ W' +Higgs). We note that both YM and W' -exchange contributions contain E^4 and E^2 terms in their amplitudes, where the E^4 terms exactly cancel between them at high energies. Thus the summation of the YM and W' -exchange given by the black curve (marked by YM+ W') contains only the remaining E^2 term in the gauge part, which is negative and will cancel against the E^2 term of Higgs-exchange amplitude (green curve). Hence, we find that the sum of all three types of contributions (given by red curve and marked by YM+ W' +Higgs), behaves like $\mathcal{O}(E^0)$ in high energy, as required by the unitarity of this renormalizable 221 model. In this plot, we compute each individual contribution from the corresponding part in $\text{Re}(a_0)$, and only the total sum (red curve) is

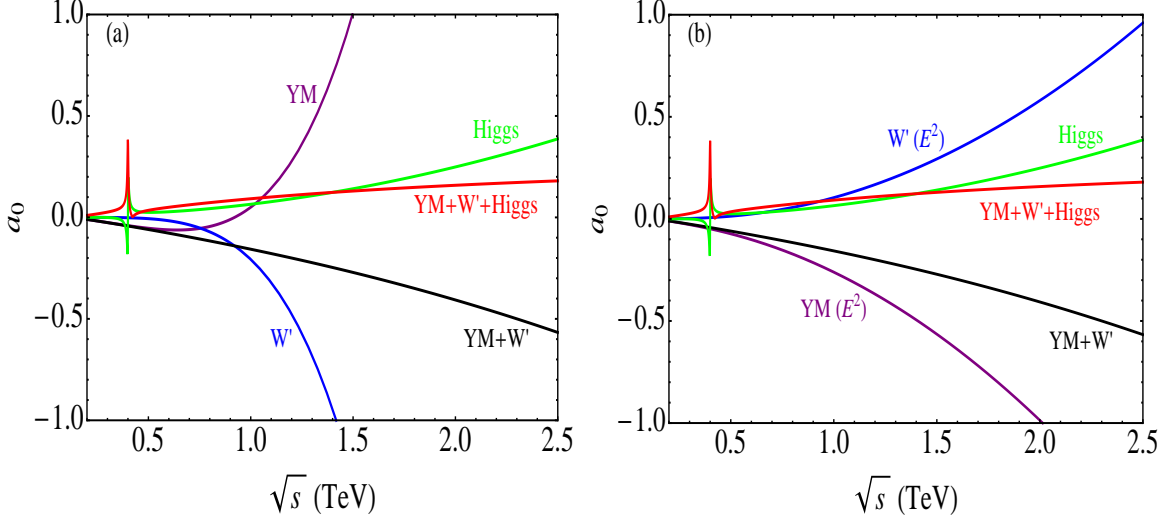


Figure 1. The s -wave amplitude $a_0(W_L W_L \rightarrow \frac{1}{\sqrt{2}} Z_L Z_L)$ as a function of scattering energy \sqrt{s} . In each plot, we have separately plotted the individual contributions from the pure Yang-Mills (YM) in purple curves (including contact terms plus W -exchange), the W' -exchange (blue curve), the h/H -exchanges (green curve), and the total sum of all three types of contributions (red curve, marked by YM+ W' +Higgs). The sum of all gauge contributions is shown by the black curve (marked by YM+ W'). The curves for individual contributions are computed from the corresponding parts in $\text{Re}(a_0)$, and only the total sum (red curve) is given in terms of $|a_0|$. Furthermore, in plot-(b) we only show the separate Yang-Mills and W' -exchange contributions for E^2 (and subleading) terms, with the asymptotic E^4 terms subtracted out, which are marked by $YM(E^2)$ and $W'(E^2)$, respectively. Both plots have the parameter inputs, $f_1 = f_2$, $(M_h, M_H) = (125, 400)\text{GeV}$, $M_{W'} = 500\text{ GeV}$, and $M_F = 2.5\text{ TeV}$.

given in terms of $|a_0|$. For Fig. 1(b), the notations are the same as plot-(a), except that we only show the separate Yang-Mills and W' -exchange contributions for E^2 (and subleading) terms, where we have subtracted out the asymptotic E^4 terms. These two contributions are marked by $YM(E^2)$ and $W'(E^2)$, respectively. From this plot, we see that the $W'(E^2)$ contribution is positive (blue curve) and much larger than the positive contribution of Higgs-exchanges (green curve) which is at most of $\mathcal{O}(E^2)$. The sum of Yang-Mills and W' -exchange (shown in black curve) is negative and its magnitude is larger than Higgs-exchange amplitude (due to the non- E^2 subleading terms). Hence, after the E^2 cancellation between YM+ W' and Higgs contributions, the final total amplitude of YM+ W' +Higgs (red curve) comes from the remaining non- E^2 subleading terms in YM+ W' contributions. In both plots, the total s -wave amplitude $|a_0|$ is the same, shown as red curves, where the s -channel resonance of the heavier Higgs boson H^0 (with a 400 GeV mass) explicitly shows up. In Fig. 1(a)-(b), we have set the inputs, $f_1 = f_2$, $(M_h, M_H) = (125, 400)\text{ GeV}$, $M_{W'} = 500\text{ GeV}$, and $M_F = 2.5\text{ TeV}$.

In Fig. 2, we further analyze the longitudinal scattering process of $W_L Z_L \rightarrow W_L Z_L$, where both s -wave and p -wave amplitudes are shown as functions of the scattering energy

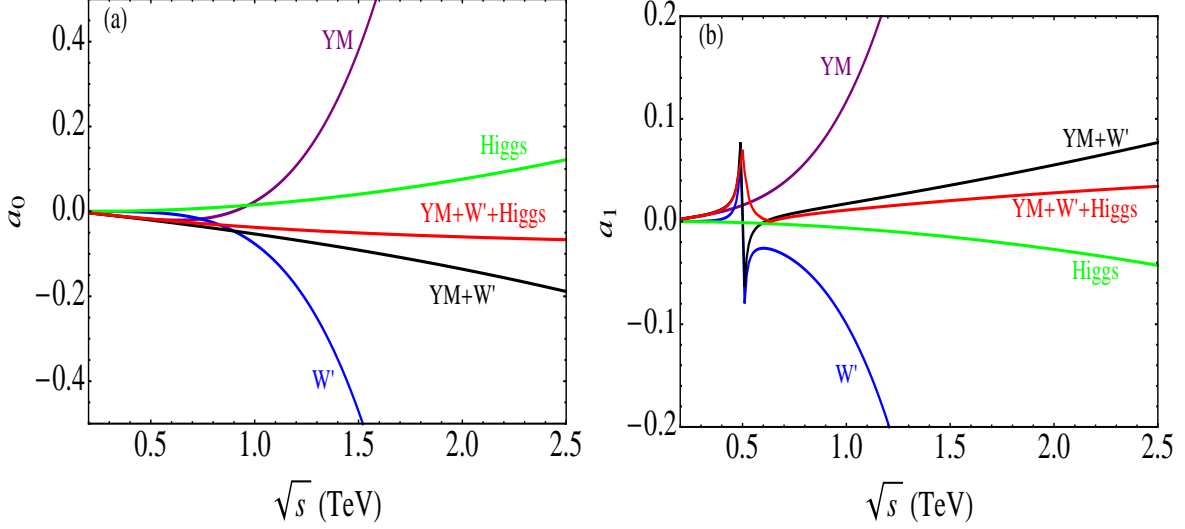


Figure 2. The s -wave amplitudes [plot-(a)] and the p -wave amplitudes [plot-(b)] for $W_L Z_L \rightarrow W_L Z_L$ scattering as functions of the scattering energy \sqrt{s} . In each panel, we have separately plotted the individual contributions from the pure Yang-Mills (YM) in purple curves (including contact terms plus W -exchange), the W' -exchange (blue curve), the h/H -exchanges (green curve), and the total sum of all three types of contributions (red curve, marked by YM+W'+Higgs). The sum of all gauge contributions is shown by the black curve (marked by YM+W'). The curves for individual contributions are computed from the corresponding parts in $\text{Re}(a_0)$. The total sum (red curve) in plot-(a) is given in terms of $\text{Re}(a_0)$, but in plot-(b) is computed for $|a_0|$. The parameter inputs are, $f_1 = f_2$, $(M_h, M_H) = (125, 400)$ GeV, $M_{W'} = 500$ GeV, and $M_F = 2.5$ TeV.

\sqrt{s} in plot-(a) and plot-(b), respectively. In both plots, we show the individual contributions from the Yang-Mills interactions (including contact terms plus W -exchange, marked by YM in purple curve), the W' -exchange (marked by W' in blue curve) and the Higgs-exchanges (marked by Higgs in green curve). The sum of YM and W -exchange contributions is depicted by the black curve (marked by YM+W'), where the E^4 terms are exactly canceled out between them, and only the E^2 (and subleading) terms are contained in the black curve. Then, we see that the two E^2 contributions in the negative YM+W' amplitude (black curve) and positive Higgs amplitude (green curve) cancel each other exactly at high energies, while the remaining terms have the asymptotic behavior of $\mathcal{O}(E^0)$, as shown in the red curve (marked by YM+W'+Higgs), which is negative since it is dominated by the YM+W' contribution. Here all curves (including the red curve) are computed from the corresponding parts of the real s -wave amplitude $\text{Re}(a_0)$. We choose the same parameter inputs of VEVs, Higgs masses, W' mass and heavy fermion masses as in Fig. 1. For Fig. 2(b), we compute the p -wave amplitude,

$$a_1(s) = \frac{1}{32\pi} \int_{-1}^1 d(\cos \theta) \cos \theta \mathcal{M}(s, \theta), \quad (2.39)$$

for the same process $W_L Z_L \rightarrow W_L Z_L$. Here all the notations and inputs are the same as those in Fig. 1(b), except that we are computing the p -wave for $W_L Z_L \rightarrow W_L Z_L$ scattering. Different from Fig. 2(a) and Fig. 1 for the s -wave amplitudes, we see from Fig. 2(b) that the Higgs-exchange amplitude becomes negative and the YM+ W' contribution is positive; and they cancel each other for the asymptotic E^2 terms. In consequence, the total sum of the p -wave amplitude is shown in the red curve (marked by YM+ W' +Higgs), which has good high energy behavior of $\mathcal{O}(E^0)$. In the plot-(b), we find that the s -channel spin-1 resonance of W' gauge boson shows up in the p -wave amplitude at 500 GeV, as expected.

Next, we analyze the unitarity bound on the heavy Higgs mass. In the above we have demonstrated how the E^4 and E^2 terms are separately canceled out in the longitudinal scattering amplitudes at high energies, and the crucial role played by the W'/Z' -exchanges and Higgs-exchanges together in the E^2 cancellation to ensure the unitarity of the model. The remaining terms in the scattering amplitudes are of $\mathcal{O}(E^0)$ and are dominated by the Higgs self-couplings related to the Higgs boson masses. Given the light Higgs boson mass of $M_h = 125$ GeV as observed by the LHC [3, 4], we can further derive an upper bound on the mass of heavier Higgs state H^0 . For this purpose, it is extremely convenient to use the equivalence theorem and analyze the corresponding Goldstone boson scattering amplitudes at high energies. Here the external in/out states (either gauge bosons or Goldstone bosons) can be treated as massless, and only the quartic contact interactions among the Goldstone and Higgs bosons can contribute to the leading scattering amplitudes at $\mathcal{O}(E^0)$. This means to take the limit $g_0, g_2 \simeq 0$. We also note that the other gauge coupling g_1 of $SU(2)_1$ may be sizable since (W', Z') gauge bosons are relatively heavy. Thus, the scattering amplitudes via the (W', Z') -exchanges may be comparable to the contact interactions. In the following, we shall estimate the unitarity bounds on the mass of the heavier Higgs state H^0 both without and with the (W', Z') contributions.

We note that the Higgs potential (2.3) enjoys a global $O(4) \otimes O(4)$ symmetry, under which two Higgs doublets Φ_1 and Φ_2 transform as $(\mathbf{4}, \mathbf{1})$ and $(\mathbf{1}, \mathbf{4})$, respectively. Hence we perform the coupled channel analysis by defining the normalized singlet two-body states under $O(4) \otimes O(4)$,

$$|X_j\rangle = \frac{1}{\sqrt{8}} \left(|h_j h_j\rangle + |\pi_j^2\rangle \right), \quad (2.40)$$

where $j = 1, 2$. Thus, we compute the coupled-channel scattering amplitudes of $|X_j\rangle \rightarrow |X_{j'}\rangle$ in terms of the 2×2 matrix,

$$\mathcal{T} = \begin{pmatrix} \langle X_1 | T | X_1 \rangle & \langle X_1 | T | X_2 \rangle \\ \langle X_2 | T | X_1 \rangle & \langle X_2 | T | X_2 \rangle \end{pmatrix}, \quad (2.41)$$

where we derive the $\mathcal{O}(E^0)$ leading contributions to its elements as follows,

$$\langle X_j | T | X_j \rangle = -3\lambda_j, \quad \langle X_1 | T | X_2 \rangle = \langle X_2 | T | X_1 \rangle = -2\lambda_{12}. \quad (2.42)$$

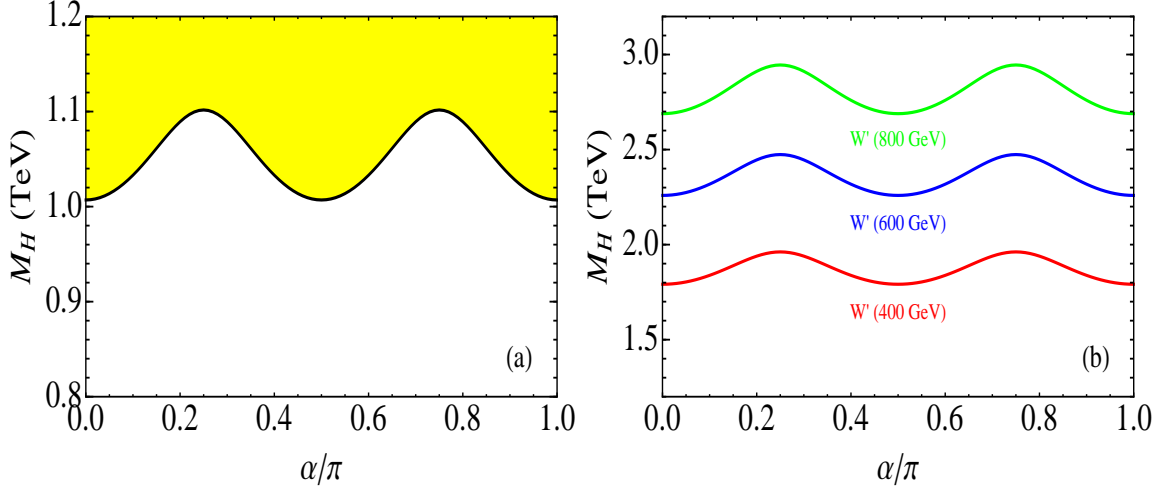


Figure 3. Unitarity bound on the heavier Higgs boson mass M_H as a function of the Higgs mixing angle α . We present the unitarity bounds by taking the contact-term contributions alone in plot-(a), and by including both contact-term and W'/Z' -exchanges in plot-(b) for three inputs of $M_{W'}$. The yellow region in plot-(a) is excluded, while in plot-(b) the region above each curve is excluded for the given input of $M_{W'}$. In both plots, we set the lighter Higgs boson mass $M_h = 125$ GeV and the Higgs VEV ratio $r = 1$.

Diagonalizing the matrix (2.41), we derive the maximal eigenvalue for the corresponding s -wave amplitude from the scalar contact interactions,

$$a_0^{\max}[\text{contact}] = -\frac{1}{32\pi} \left[3(\lambda_1 + \lambda_2) + \sqrt{9(\lambda_1 - \lambda_2)^2 + 16\lambda_{12}^2} \right], \quad (2.43)$$

which is a function of the three quartic Higgs self-couplings $(\lambda_1, \lambda_2, \lambda_{12})$, which is expected to give the best bound on the Higgs mass under the s -wave unitarity condition, $|\text{Re } a_0^{\max}| < \frac{1}{2}$. As we noted in Sec. 2.2, fixing the two VEVs, the three Higgs self-couplings $(\lambda_1, \lambda_2, \lambda_{12})$ can be equivalently expressed in terms of the two Higgs masses and one mixing angle, (M_h, M_H, α) . Hence, inputting the observed lighter Higgs boson mass $M_h = 125$ GeV and Higgs VEV ratio $r = 1$, we can derive the upper bound on the heavier Higgs boson mass M_H as a function of the Higgs mixing angle α . We present our findings in Fig. 3(a). We see that to respect the unitarity over the full range of mixing angle α imposes the following bound on the mass of the Higgs boson H^0 ,

$$M_H \leq 1.0 \text{ TeV}. \quad (2.44)$$

Furthermore, Fig. 3(a) shows that this unitarity limit could become weaker for some ranges of α , but we find that the bound is only slightly weakened to $M_H \leq 1.10$ TeV.

Including the W'/Z' -exchanges for the coupled channel amplitudes under the limit of

$g_0, g_2 \simeq 0$, we extend the elements of the S -matrix (2.41) as follows,

$$\langle X_j|T|X_j \rangle = -3\lambda_j + (\delta_a + \delta_b), \quad (2.45a)$$

$$\langle X_1|T|X_2 \rangle = \langle X_2|T|X_1 \rangle = -2\lambda_{12} + \delta_a, \quad (2.45b)$$

$$\delta_a = \frac{g_1^2}{8} \frac{s \cos \theta}{s - M_{W'}^2}, \quad (2.45c)$$

$$\delta_b = \frac{g_1^2}{16} \left[\frac{7(3 + \cos \theta)}{(1 - \cos \theta) + 2M_{W'}^2/s} + \frac{5(3 - \cos \theta)}{(1 + \cos \theta) + 2M_{W'}^2/s} \right]. \quad (2.45d)$$

Accordingly, we find the modified maximal eigenvalue for the s -wave amplitude,

$$\widehat{a}_0^{\max} = a_0^{\max}[\text{contact}] + \frac{1}{16\pi} \Delta, \quad (2.46a)$$

$$\Delta = \frac{3g_1^2}{4} \left[\left(2 + \frac{M_{W'}^2}{s} \right) \log \left(1 + \frac{s}{M_{W'}^2} \right) - 1 \right], \quad (2.46b)$$

where $a_0^{\max}[\text{contact}]$ is the contribution of contact terms as in (2.43), and the Δ term arises from the W'/Z' -exchanges. We note that the W'/Z' -exchanges partially cancel the contact term contributions. Imposing the s -wave unitarity condition of $|\text{Re} \widehat{a}_0^{\max}| < \frac{1}{2}$ thus further relaxes the M_H upper bound as compared to the contact-terms alone in Fig. 3(a). This is explicitly displayed in Fig. 3(b) with the center-of-mass energy being $\sqrt{s} = 5$ TeV for three sample inputs of $M_{W'} = (400, 600, 800)$ GeV and $r = 1$. Accordingly, we infer the mass bounds on the Higgs boson H^0 over the full range of mixing angle α ,

$$\begin{aligned} M_{W'} = 400 \text{ GeV}: \quad M_H &\leq 1.80 \text{ TeV}, \\ M_{W'} = 600 \text{ GeV}: \quad M_H &\leq 2.26 \text{ TeV}, \\ M_{W'} = 800 \text{ GeV}: \quad M_H &\leq 2.69 \text{ TeV}. \end{aligned} \quad (2.47)$$

3 LHC Signatures of the Lighter Higgs Boson h^0

In this section, we study the production and decays of the light Higgs boson h^0 at the LHC, based upon its non-SM couplings presented in the previous section.

3.1 Decay Branching Fractions of h^0

There are three types of the decay processes for the light Higgs boson h^0 in the current 221 model. This includes: (i) decays into the SM fermions; (ii) decays into WW^* or ZZ^* ; and (iii) the loop-induced decays into $\gamma\gamma$, γZ , or gg . Due to the non-SM couplings of h^0 in Sec. 2.4, the partial decay widths of h^0 differ from the SM values [27] and are explicitly given

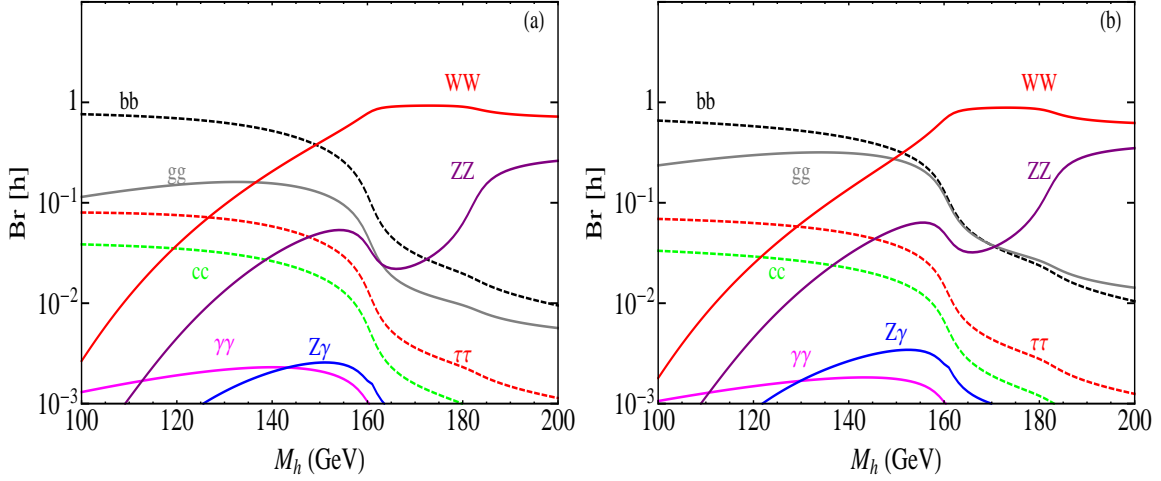


Figure 4. Decay branching fractions of the light Higgs boson h^0 over the mass-range $100 < M_h < 200$ GeV. We have input $f_1 = f_2$ and $(M_{W'}, M_F) = (0.6, 2.5)$ TeV. The Higgs mixing angle is taken to be $\alpha = 0.8\pi$ in plot-(a) and $\alpha = 0.2\pi$ in plot-(b), respectively.

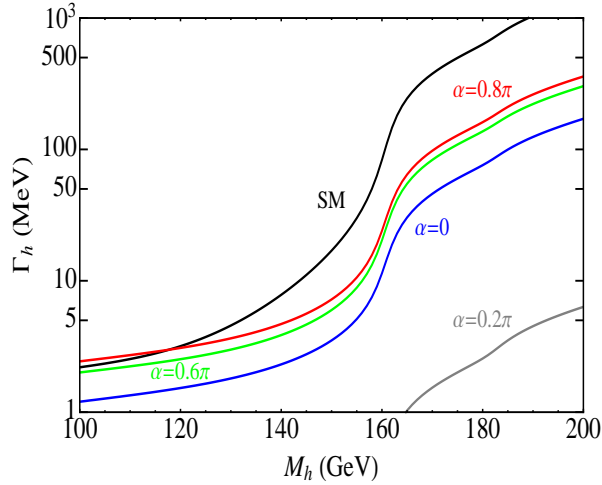


Figure 5. Total decay width of the light CP-even Higgs boson h^0 with $\alpha = 0.8\pi$ (red), $\alpha = 0.6\pi$ (green), $\alpha = 0$ (blue) and $\alpha = 0.2\pi$ (grey), over the mass-range $100 - 200$ GeV. For comparison, the total width of the SM Higgs boson is depicted in the same mass-range (black curve). We set the other inputs as, $f_1 = f_2$ and $(M_{W'}, M_F) = (0.6, 2.5)$ TeV.

in the Appendix A. In particular, the W' -loop induced contributions can enhance the $\gamma\gamma$ and $Z\gamma$ partial widths over the proper parameter space of our model.⁵

From these, we compute the decay branching fractions of h^0 into the SM final states. In

⁵Very recently, the W' -loop contribution to the diphoton channel was also studied for different models [28]; and possible enhancements of the diphoton rate for some composite Higgs models and analysis of their $\pi\pi$ scattering channels were discussed in [29].

Fig. 4, we plot h^0 branching ratios over the mass range of $100 \text{ GeV} < M_h < 200 \text{ GeV}$. For illustration, we take $f_1 = f_2$, $M_{W'} = 600 \text{ GeV}$, and $M_F = 2.5 \text{ TeV}$, with different values of $\alpha = 0.2\pi$ and $\alpha = 0.8\pi$, respectively. For comparison, we show the total decay widths for our h^0 Higgs boson and the SM Higgs boson in Fig. 5. For the lighter h^0 , we plot the total width of h^0 for four values of the mixing parameter $\alpha = 0, 0.2\pi, 0.6\pi, 0.8\pi$, respectively. We see that for $\alpha = 0.8\pi$ and $\alpha = 0.6\pi$, the total widths vary very little, while they both become visibly smaller than the SM values for the Higgs mass above 120 GeV . Besides, Fig. 5 shows that our h^0 width with $\alpha = 0.2\pi$ is substantially lower than the SM. We have further verified that the main features of Fig. 5 still remain by varying the inputs of the VEV ratio f_2/f_1 and heavy masses ($M_{W'}, M_F$).

3.2 Signatures of h^0 via Gluon Fusion

The gluon fusion process gives the dominant Higgs production mechanism at the LHC. It is induced by colored particles at the loop-level. For the SM case, only the top-quark loop contribution dominates. But for the present model, we have six extra vector-like heavy partners of the SM quarks with masses $> 1.8 \text{ TeV}$, which will contribute to the gluon fusions as well. The ratio of the gluon fusion cross sections between the 221 model and the SM is

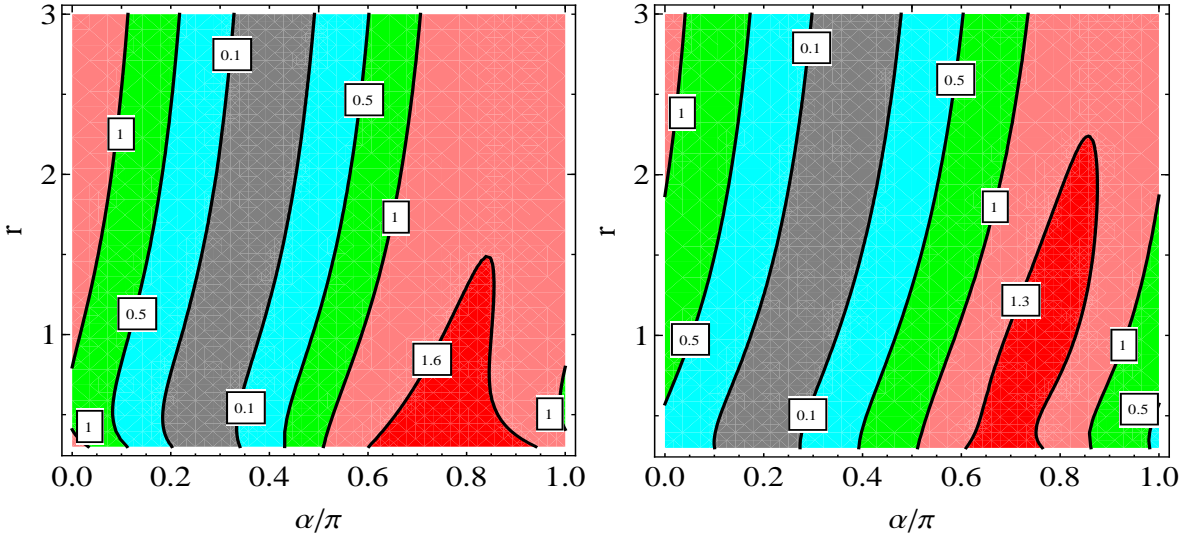


Figure 6. Contour plots of the gluon-fusion ratio \mathcal{R}_{ggh} in the parameter space of r versus α , with light Higgs mass $M_h = 125 \text{ GeV}$. Different ranges of \mathcal{R}_{ggh} are represented by the colored bands: $\mathcal{R}_{ggh} < 0.1$ (gray), $0.1 < \mathcal{R}_{ggh} < 0.5$ (light-blue), $0.5 < \mathcal{R}_{ggh} < 1$ (green), $1 < \mathcal{R}_{ggh} < 1.6$ (1.3) (pink), and $\mathcal{R}_{ggh} > 1.6$ (1.3) (red). We have input $M_{W'} = 400 \text{ GeV}$ for the left panel and $M_{W'} = 600 \text{ GeV}$ for the right panel. The heavy fermion mass is set as $M_F = 2.5 \text{ TeV}$ for both panels. The maximal enhancement factors are $\mathcal{R}_{ggh} \simeq 1.7$ (left panel) and $\mathcal{R}_{ggh} \simeq 1.3$ (right panel), respectively.

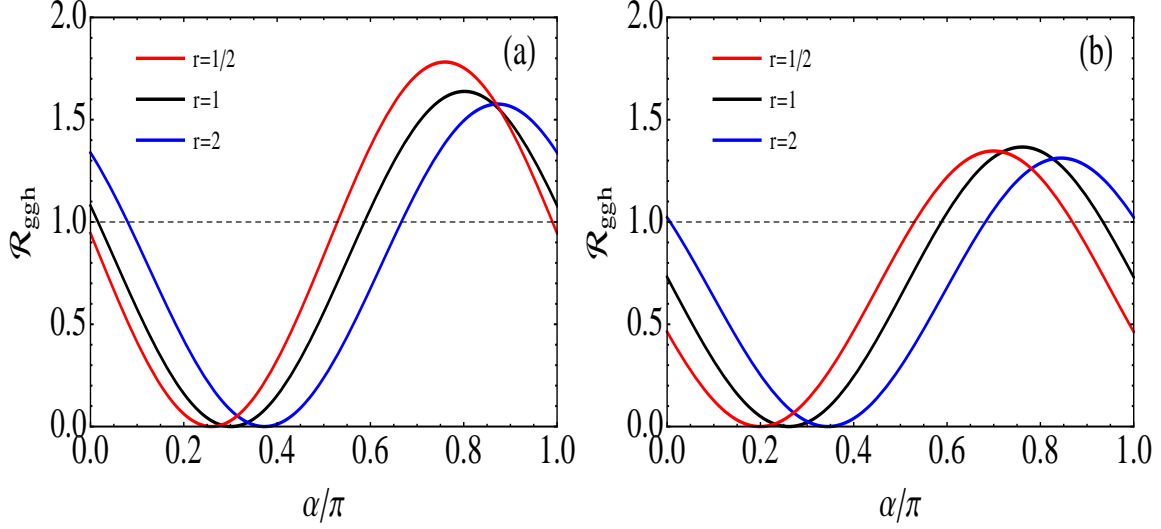


Figure 7. Ratio \mathcal{R}_{ggh} of h^0 production cross sections via gluon fusion process as a function of Higgs mixing angle α . We identify the lighter Higgs mass $M_h = 125$ GeV and set the heavy fermion mass $M_F = 2.5$ TeV for both plots. The panels (a) and (b) have input $M_{W'} = 400$ GeV and $M_{W'} = 600$ GeV, respectively. We have varied the VEV ratio, $r = (\frac{1}{2}, 1, 2)$, in each plot.

readily given by the ratio between the partial decay widths of $h \rightarrow gg$ in Eq. (A.3),

$$\mathcal{R}_{ggh} \equiv \frac{\sigma[gg \rightarrow h]}{\sigma[gg \rightarrow h]_{\text{SM}}} = \frac{\Gamma[h \rightarrow gg]}{\Gamma[h \rightarrow gg]_{\text{SM}}}. \quad (3.1)$$

We analyze this ratio over the parameter space of (α, r) , where α is the Higgs mixing angle and the VEV ratio $r = f_2/f_1$ is shown for the range of $r = (0.5, 2) = O(1)$.

In Fig. 6, we present the contour plots of the gluon-fusion ratio \mathcal{R}_{ggh} over the parameter space of (α, r) . With the generic parameter inputs, we find that this ratio can be either moderately enhanced or quite suppressed, which periodically depends on the Higgs boson mixing angle $\alpha \in [0, \pi)$. Here for most choices of the mixing angle α , the gluon fusion ratio \mathcal{R}_{ggh} is not so sensitive to the VEV ratio r since most \mathcal{R}_{ggh} contours in Fig. 6 are approximately vertical bands. In Fig. 6, we see that the ratio \mathcal{R}_{ggh} reaches the peak values for relatively large mixing angle $\alpha \simeq (0.6 - 0.9)\pi$ and smaller VEV ratio $r \lesssim 2$, as marked by the red regions in both plots. For these red regions of Fig. 6, we find that $\mathcal{R}_{ggh} \simeq 1.6 - 1.8$ in the left panel, and $\mathcal{R}_{ggh} \simeq 1.3$ in the right panel. In the following analyses, we will take $r = \frac{1}{2}, 2$ as two sample inputs, and compare them with the $r = 1$ choice (with equal VEVs).

In Fig. 7(a)-(b), we further display the gluon-fusion ratio \mathcal{R}_{ggh} as a function of the Higgs mixing angle α , for the parameter inputs $M_h = 125$ GeV and $M_F = 2.5$ TeV. The plots (a) and (b) have input $M_{W'} = 400$ GeV and $M_{W'} = 600$ GeV, respectively. In each panel, we have varied the VEV ratio, $r = (\frac{1}{2}, 1, 2)$. We see that these production cross sections can be reasonably enhanced relative to the SM. They are highly correlated with the top-quark

Yukawa coupling to the Higgs boson. The maximum values of the ratio \mathcal{R}_{ggh} reach around $\alpha = (0.7 - 0.9)\pi$, depending on the VEV ratio r . From (2.25), we see that $G_{\bar{t}th} \approx G_{\bar{t}th}^{\text{SM}}$ for $r = 1$. This ratio \mathcal{R}_{ggh} may also vanish at some other points, around $\alpha = (0.2 - 0.35)\pi$, where the top-quark Yukawa coupling $G_{\bar{t}th}$ becomes nearly vanishing. Comparing the two plots of Fig. 7, we see that \mathcal{R}_{ggh} gets reduced as $M_{W'}$ becomes larger. This is a consequence from the suppression of heavy fermion Yukawa coupling, $\xi_{hFF} = \mathcal{O}(m_W^2/M_{W'}^2)$. In each plot, we also show the effects of different VEV ratios around $r = \mathcal{O}(1)$, which are consistent with the contours in Fig. 6.

Next, we study the LHC signals of light Higgs boson h^0 via the most sensitive channels ($\gamma\gamma$, WW^* , ZZ^*). The signals is determined by the product of production cross section and decay branching fraction. It is convenient to analyze signal ratios between our prediction and the SM expectation,

$$\mathcal{R}_{XX} \equiv \frac{\sigma[gg \rightarrow h] \times \text{Br}[h \rightarrow XX]}{\sigma[gg \rightarrow h]_{\text{SM}} \times \text{Br}[h \rightarrow XX]_{\text{SM}}}. \quad (3.2)$$

In Fig. 8, for the light Higgs boson h^0 with mass $M_h = 125 \text{ GeV}$, we plot each ratio of ($\mathcal{R}_{\gamma\gamma}$, \mathcal{R}_{WW} , \mathcal{R}_{ZZ}) as a function of Higgs mixing angle α . The input parameters are set to be, $M_{W'} = 400 \text{ GeV}$ (600 GeV), and $M = 2.5 \text{ TeV}$ for the plot-(a) [plot-(b)]. In both plots, we have displayed the measured ($\gamma\gamma$, WW , ZZ) rates by the ATLAS and CMS experiments [3, 4], with central values plus the $\pm 1\sigma$ error bars. These are shown by the vertical gray lines, marked with ($\gamma\gamma_A$, ZZ_A , WW_A) and ($\gamma\gamma_C$, ZZ_C , WW_C). Here the subscripts “A” and “C” denote the ATLAS and CMS data respectively, which do not depend on α in the horizontal direction.

The predicted $h^0 \rightarrow \gamma\gamma$ signals can be larger than the SM Higgs boson with the same mass $M_h = 125 \text{ GeV}$, depending on the mixing angle α . For $M_{W'} = 400 \text{ GeV}$, Fig. 8(a) shows that $\mathcal{R}_{\gamma\gamma} > 1$ holds for $0.60\pi < \alpha < 0.97\pi$. For $M_{W'} = 600 \text{ GeV}$, Fig. 8(b) shows that $\mathcal{R}_{\gamma\gamma} > 1$ holds for $0.65\pi < \alpha < 0.9\pi$. We see that for the $\gamma\gamma$ channel, the maximal enhancement $\mathcal{R}_{\gamma\gamma} = 1.4$ for $M_{W'} = 400 \text{ GeV}$, and becomes $\mathcal{R}_{\gamma\gamma} = 1.2$ for $M_{W'} = 600 \text{ GeV}$. They are both consistent with the current LHC data as shown in Fig. 8. The upcoming data from the LHC (8 TeV) and the next phase of LHC (14 TeV) will further discriminate this non-standard Higgs boson h^0 from the SM.

We also note that the $Z\gamma$ signals are generally suppressed relative to the di-photon channel, which are reduced by the phase space suppression. The $Z\gamma$ signals also become smaller for heavier W' . This can be seen from inspecting the form factors in (A.10e) and (A.10f).

Signal rates in the WW^* and ZZ^* channels are quite close to each other, and the minor differences originate from the $\mathcal{O}(x^2)$ terms in Eq. (2.24). Fig. 8 further shows that the \mathcal{R}_{VV} ratios are smaller than one over the full range of α and for $f_1 = f_2$.⁶ This is because the

⁶The ratio $\mathcal{R}_{VV} \sim 1$ could be realized for other situation with $f_1 \gg f_2$ or $f_1 \ll f_2$. But this would make W'/Z' masses too heavy, well above 1 TeV, and thus irrelevant to the unitarity restoration. So this is not the parameter space we will consider for our 221 model, as we mentioned in Sec. 2.

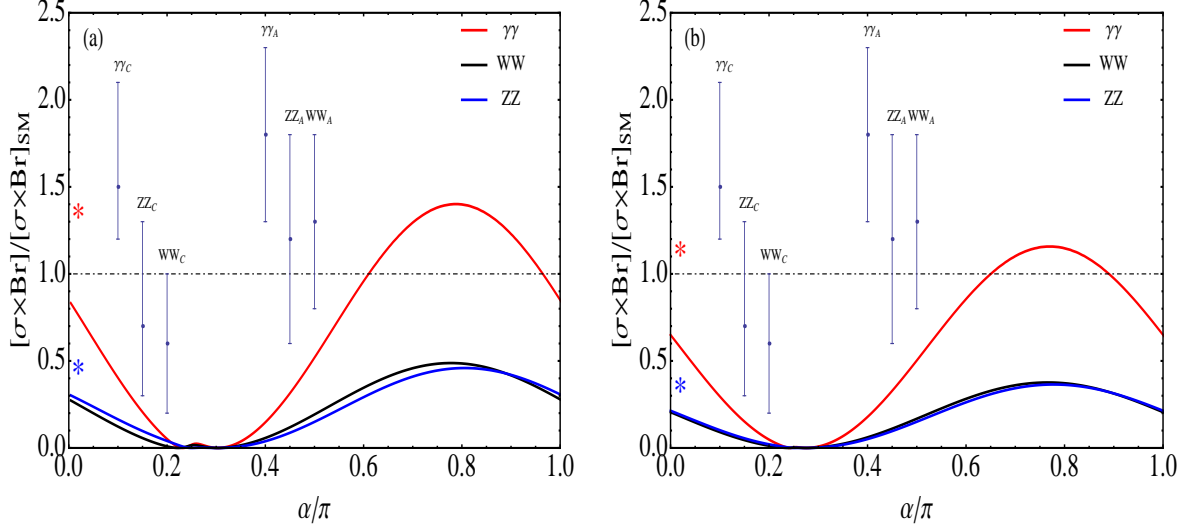


Figure 8. Signal ratios ($\mathcal{R}_{\gamma\gamma}$, \mathcal{R}_{WW} , \mathcal{R}_{ZZ}) as functions of the Higgs mixing angle α . We set $M_h = 125$ GeV and input $f_1 = f_2$. The heavy masses are taken to be, $M_F = 2.5$ TeV and $M_{W'} = 400$ GeV [plot-(a)] or $M_{W'} = 600$ GeV [plot-(b)]. In each plot, at $\alpha = 0$, we also show an interesting sample with degenerate h^0 and H^0 , where the predicted $\gamma\gamma$ rate is marked by the red asterisk and the ZZ^* (WW^*) rate is marked by the blue asterisk. The ATLAS and CMS data for $\gamma\gamma$, ZZ^* , and WW^* channels [5, 6] are shown for each plot, where the subscripts “A” and “C” stand for ATLAS and CMS, respectively. These data points do not depend on α and their horizontal locations have no physical meaning, except for the convenience of presentation.

WW_h and ZZ_h couplings of (2.24) are always suppressed relative to the SM couplings. Fig. 8 shows that the maximal WW^* and ZZ^* signals can reach about $\frac{1}{3} - \frac{1}{2}$ of the SM expectations.

We further vary the input of VEV ratios according to (2.23). Different from Fig. 8 with $r = f_2/f_1 = 1$, we redo the analysis in Fig. 9(a) and 9(b) by inputting $r = \frac{1}{2}$ and $r = 2$, respectively. The heavy masses are taken as, $M_{W'} = 400$ GeV and $M_F = 2.5$ TeV, for both plots. The signals via the WW^* and ZZ^* channels exhibit stronger dependence on the VEV ratio r than the di-photon channel. Especially, in contrast to Fig. 8(a), we see from Fig. 9(a)-(b) that for $r = \frac{1}{2}$ ($r = 2$), the maximal ratio of WW^* rate over the SM has raised to about 1.0 (0.9), and that of ZZ^* mode is shifted up to 0.8 (0.9), while the maximal $\gamma\gamma$ signals become about a factor 1.6 (1.4) of the SM expectation. These predictions are in perfect agreement with the current LHC data shown in the same figure.

Based on our analysis in the previous section, we present an interesting case under $\lambda_1 f_1^2 = \lambda_2 f_2^2$ and $\lambda_{12} = 0$, where two Higgs bosons (h^0 , H^0) become degenerate in mass, so we have $M_h = M_H = 125$ GeV. This corresponds to the Higgs mixing angle $\alpha = 0$. In practice, we can allow the masses of (h^0 , H^0) to be nearly degenerate, consistent with the present mass-difference and uncertainties of the 125 – 126 GeV resonances found in the ATLAS and

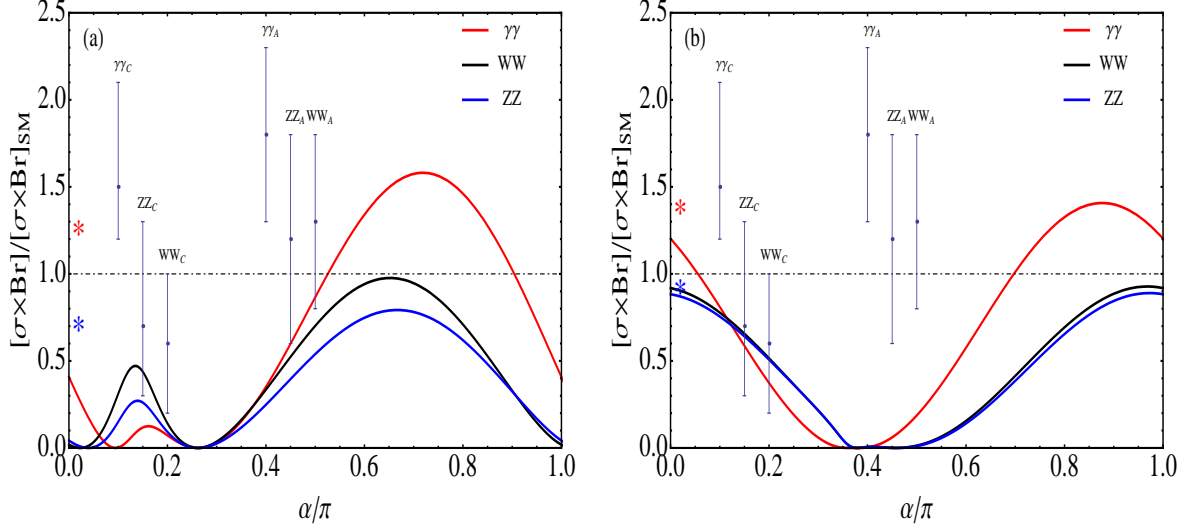


Figure 9. Signal ratios ($\mathcal{R}_{\gamma\gamma}$, \mathcal{R}_{WW} , \mathcal{R}_{ZZ}) as functions of the Higgs mixing angle α . The inputs are the same as Fig 8, except we set $f_2/f_1 = 1/2$ in plot-(a) and $f_2/f_1 = 2$ in plot-(b). For both panels we take $M_{W'} = 400$ GeV. In each plot, at $\alpha = 0$, we also show an interesting sample with degenerate h^0 and H^0 , where the predicted $\gamma\gamma$ rate is marked by the red asterisk and the ZZ^* (WW^*) rate is marked by the blue asterisk. The ATLAS and CMS data for $\gamma\gamma$, ZZ^* , and WW^* channels [5, 6] are shown for each plot, where the subscripts “A” and “C” stand for ATLAS and CMS, respectively. These data points do not depend on α and their horizontal locations have no physical meaning, except for the convenience of presentation.

CMS detectors [3, 4]. According to the formulae of (2.24)-(2.25), we note that for $\alpha = 0$, the Higgs couplings with gauge bosons and fermions take the simple relations, $\xi_{hVV}/\xi_{HVV} \simeq r^3$, $\xi_{hff}/\xi_{Hff} \simeq r$, and $\xi_{hFF}/\xi_{HFF} \simeq -[r/(1+r^2)^2](x^4 M_F^2/m_f^2)$. Numerically, we show the degeneracy signals for the $\gamma\gamma$ and ZZ^*/WW^* channels in Figs. 8-9, where the red asterisks represent the predictions for the $\gamma\gamma$ mode and the blue asterisks denote the results for the ZZ^* (WW^*) mode. To summarize, we present the predicted signal rates for the degeneracy samples, with $r = 1$,

$$\mathcal{R}_{\gamma\gamma}^{\text{deg}} = 1.37, \quad \mathcal{R}_{ZZ}^{\text{deg}} = 0.46, \quad \mathcal{R}_{WW}^{\text{deg}} = 0.47, \quad (\text{for } M_{W'} = 400 \text{ GeV, } r = 1); \quad (3.3a)$$

$$\mathcal{R}_{\gamma\gamma}^{\text{deg}} = 1.15, \quad \mathcal{R}_{ZZ}^{\text{deg}} = 0.36, \quad \mathcal{R}_{WW}^{\text{deg}} = 0.37, \quad (\text{for } M_{W'} = 600 \text{ GeV, } r = 1). \quad (3.3b)$$

and with $r = \frac{1}{2}, 2$,

$$\mathcal{R}_{\gamma\gamma}^{\text{deg}} = 1.27, \quad \mathcal{R}_{ZZ}^{\text{deg}} = 0.58, \quad \mathcal{R}_{WW}^{\text{deg}} = 0.72, \quad (\text{for } M_{W'} = 400 \text{ GeV, } r = \frac{1}{2}); \quad (3.4a)$$

$$\mathcal{R}_{\gamma\gamma}^{\text{deg}} = 1.39, \quad \mathcal{R}_{ZZ}^{\text{deg}} = 0.89, \quad \mathcal{R}_{WW}^{\text{deg}} = 0.93, \quad (\text{for } M_{W'} = 400 \text{ GeV, } r = 2). \quad (3.4b)$$

It is clear that they agree well with the current LHC observations, and can be further discriminated from the SM Higgs boson. In passing, during the finalization of this paper, we

notice a different study appeared [30], which considered the two nearly degenerate neutral Higgs bosons in the context of GUT-scale NMSSM scenarios and found enhanced $\gamma\gamma$ signal rate as well as broadened mass peaks. Our collider phenomena with the nearly degenerate (h^0, H^0) differs from [30] substantially, due to the new gauge bosons and vector-like heavy fermions, as well as the absence of charged Higgs boson and superpartners in our model.

3.3 Signatures of h^0 via Associated Production and Vector Boson Fusion

We now turn to discussing the other two production channels, the associated production process $q_1\bar{q}_2 \rightarrow Vh$ and the vector boson fusion (VBF) process $q_1q_2 \rightarrow hq_3q_4$. In both productions, the hVV couplings and the decay branching fractions of h^0 differ from the SM Higgs boson. Let us consider the Higgs decays into the SM fermions $h^0 \rightarrow f\bar{f}$, with the final states such as $f\bar{f} = b\bar{b}, \tau\bar{\tau}$. Using the couplings from (2.24), (2.25) and (2.31), we can derive the signal ratios of the current model over the SM as follows,

$$\frac{\sigma[q_1\bar{q}_2 \rightarrow Vh] \times \text{Br}[h \rightarrow f\bar{f}]}{\sigma[q_1\bar{q}_2 \rightarrow Vh]_{\text{SM}} \times \text{Br}[h \rightarrow f\bar{f}]_{\text{SM}}} \simeq \xi_{hVV}^2 \xi_{hff}^2 \frac{\Gamma_h^{\text{SM}}}{\Gamma_h}, \quad (3.5a)$$

$$\frac{\sigma[q_1q_2 \rightarrow hq_3q_4] \times \text{Br}[h \rightarrow f\bar{f}]}{\sigma[q_1q_2 \rightarrow hq_3q_4]_{\text{SM}} \times \text{Br}[h \rightarrow f\bar{f}]_{\text{SM}}} \simeq \xi_{hVV}^2 \xi_{hff}^2 \frac{\Gamma_h^{\text{SM}}}{\Gamma_h}, \quad (3.5b)$$

where the relevant $V-q-\bar{q}'$ couplings equal the SM couplings to good accuracy (cf. Sec. 2.4.2) and the small $\mathcal{O}(x^4)$ corrections can be safely dropped here. Hence, with (2.24) and (2.25), we derive coupling ratio on the RHS of (3.5),

$$\xi_{hVV}^2 \xi_{hff}^2 \simeq \frac{(r^3 c_\alpha - s_\alpha)^2 (r c_\alpha - s_\alpha)^2}{(1 + r^2)^4}, \quad (3.6)$$

which only explicitly depends on the VEV ratio $r = f_2/f_1$ and Higgs mixing angle α . For the current analysis, we will vary r within $\mathcal{O}(1)$. Meanwhile it is useful to note the two special limits, $r \rightarrow 0$ and $r \rightarrow \infty$. For $r \rightarrow 0$ ($f_1 \gg f_2$), we have $\xi_{hVV}^2 \xi_{hff}^2 \rightarrow \sin^4 \alpha$; while for $r \rightarrow \infty$ ($f_2 \gg f_1$), we arrive at $\xi_{hVV}^2 \xi_{hff}^2 \rightarrow \cos^4 \alpha$.

In Fig. 10, we plot the ratios (3.5)-(3.6) for the present model as a function of the Higgs mixing angle α . We identify the lighter Higgs boson mass $M_h = 125$ GeV and choose the heavy fermion mass $M = 2.5$ TeV. In the plots (a) and (b) we have input $M_{W'} = 400$ GeV and $M_{W'} = 600$ GeV, respectively. In each plot, we have varied the VEV relations, $f_2 = f_1/2$, $f_2 = f_1$, and $f_2 = 2f_1$, corresponding to $r = (\frac{1}{2}, 1, 2)$, respectively. Inspecting each panel, we note that for smaller r such as $r = \frac{1}{2}$, the curve is similar to the asymptotic behavior $\sin^4 \alpha$ (under $r \rightarrow 0$), while for larger r such as $r = 2$, the curve becomes closer to the asymptotic behavior $\cos^4 \alpha$ (under $r \rightarrow \infty$). As expected, our signals are always smaller than the SM expectation due to the general suppressions in the tree-level hVV and hff couplings of (2.24)-(2.25). From Fig. 10, we see that for the VEV ratio r varying within $\mathcal{O}(1)$, the h^0 signal rates can reach up to about $\frac{1}{3} - \frac{3}{4}$ of the SM expectations.

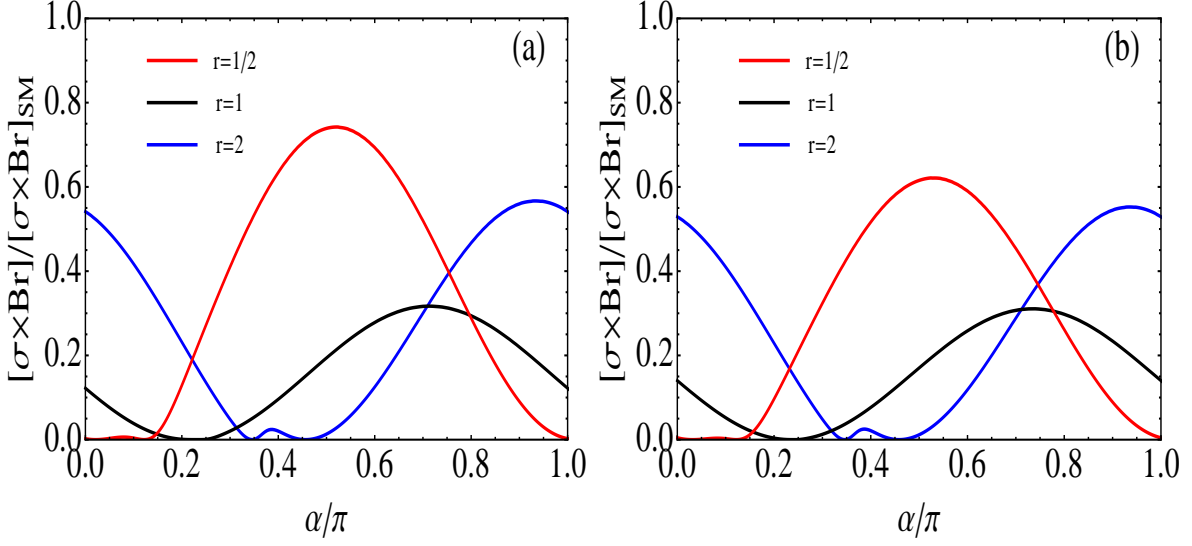


Figure 10. Signals of $\sigma(q\bar{q}' \rightarrow Vh) \times \text{Br}(h \rightarrow b\bar{b})$ or $\sigma(q\bar{q}' \rightarrow h q_3 q_4) \times \text{Br}(h \rightarrow \tau\bar{\tau})$ in the present model over the corresponding SM expectations, as a function of the Higgs mixing angle α . We identify the lighter Higgs mass $M_h = 125$ GeV and set the heavy fermion mass $M_F = 2.5$ TeV for both plots. The panels (a) and (b) have input $M_{W'} = 400$ GeV and $M_{W'} = 600$ GeV, respectively. We have varied the VEV ratio, $r = (\frac{1}{2}, 1, 2)$, in each plot.

Finally, we note that for the case of two (nearly) degenerate Higgs states h^0 and H^0 with masses around 125 – 126 GeV, the signals at $\alpha = 0$ will get enhanced. We summarize the corresponding maximal ratios of signal rates \mathcal{R} as follows,

$$\mathcal{R}^{\text{deg}} = (0.55, 0.32, 0.74), \quad \text{for } r = \left(2, 1, \frac{1}{2}\right) \text{ and } M_{W'} = 400 \text{ GeV}; \quad (3.7a)$$

$$\mathcal{R}^{\text{deg}} = (0.54, 0.31, 0.62), \quad \text{for } r = \left(2, 1, \frac{1}{2}\right) \text{ and } M_{W'} = 600 \text{ GeV}. \quad (3.7b)$$

These should be compared to the non-degenerate predictions of Fig. 10 for the choice of $\alpha = 0$.

4 LHC Signatures of the Heavier Higgs Boson H^0

In this section, we proceed to study the LHC signals of the heavier CP-even Higgs boson H^0 . For the SM Higgs boson in the large mass-ranges, the ATLAS experiment has excluded the SM Higgs boson mass window of (130.7, 523) GeV at 95% C.L. [3][31], while the CMS has put exclusion limit within the mass-range of (128, 600) GeV at 95% C.L. [4][32]. The dominant decay channels for a heavy SM or SM-like Higgs boson are known to be $h_{\text{SM}}^0 \rightarrow (WW, ZZ)$. For the present analysis, we will study our signal predictions of the heavier Higgs boson

H^0 through the most sensitive channels of $H \rightarrow ZZ \rightarrow 4\ell$ and $H \rightarrow WW \rightarrow 2\ell 2\nu$, in comparison with the ATLAS and CMS searches. We find parameter regions where H^0 is relatively light and well below 600 GeV, but is hidden and escapes the current LHC searches in the $H \rightarrow WW, ZZ$ channels so far. We demonstrate that the current LHC (8 TeV) is starting to probe the H^0 Higgs boson over some parameter ranges, and the next runs at LHC (14 TeV) with higher integrated luminosities will have good potential to discover or exclude H^0 over significant parameter space, providing a decisive test of this model against the conventional SM.

4.1 Decay Branching Fractions and Productions of H^0

The gauge and Yukawa couplings of H^0 Higgs boson are derived in section 2.4. For the present study, we first analyze the decay branching fractions of H^0 over the mass-range of $M_H = 130 - 600$ GeV. In Fig. 11 and Fig. 12, we compute the H^0 decay branching fractions for the VEV ratio $r = 1$ and $r = \frac{1}{2}$, respectively, where we also set the sample heavy fermion mass $M_F = 2.5$ TeV. In Figs. 11-12, we present the results with $M_{W'} = 600$ GeV for plot-(a)(b), while for plot-(c)(d), we set $M_{W'} = 400$ GeV. In addition, we input the sample value of Higgs mixing angle $\alpha = 0.6\pi$ for the plot-(a)(c) of Figs. 11-12, and $\alpha = 0.8\pi$ for their plot-(b)(d).

Over most of the parameter region, Figs. 11-12 show that the WW and ZZ final states are the dominant decay channels of H^0 . Accordingly, the detection of H^0 should be most sensitive via $gg \rightarrow H^0 \rightarrow ZZ \rightarrow 4\ell$ and $gg \rightarrow H^0 \rightarrow WW \rightarrow 2\ell 2\nu$. We note that for a lighter mass of the new gauge boson, such as $M_{W'} = 400$ GeV in plot-(c)(d) of Figs. 11-12, the decay channel $H \rightarrow VV'$ is open for $M_H > M_{V'} + m_V$. As shown in (2.27a) of Sec. 2.4, we see that the HVV' couplings receive enhancement from the heavy mass $M_{V'}$, and thus can make the $H^0 \rightarrow VV'$ decay modes significant for the large M_H mass ranges.

In addition, we can derive the cubic scalar vertex H - h - h from the Higgs potential (2.3) with the coupling,

$$G_{Hhh} = -\frac{1}{2} \sin 2\alpha \left(M_h^2 + \frac{1}{2} M_H^2 \right) \left(\frac{\cos \alpha}{f_1} + \frac{\sin \alpha}{f_2} \right). \quad (4.1)$$

Thus, when the heavy Higgs boson mass becomes $M_H \geq 2M_h$, the decay channel $H^0 \rightarrow h^0 h^0$ will be opened, with the partial decay width,

$$\Gamma[H^0 \rightarrow h^0 h^0] = \frac{G_{Hhh}^2}{8\pi M_H} \sqrt{1 - \frac{4M_h^2}{M_H^2}}. \quad (4.2)$$

By identifying the lighter Higgs boson mass $M_h = 125$ GeV, this decay mode is open for the mass-range $M_H \geq 250$ GeV. We find that the branching fraction of $H^0 \rightarrow h^0 h^0$ may be comparable to the major channels $H^0 \rightarrow WW, ZZ, tt$ in the relevant mass-range of H^0 , as shown in Fig. 11(b)(d) for $(r, \alpha) = (1, 0.8\pi)$ and Fig. 12(a)(c) for $(r, \alpha) = (\frac{1}{2}, 0.6\pi)$.

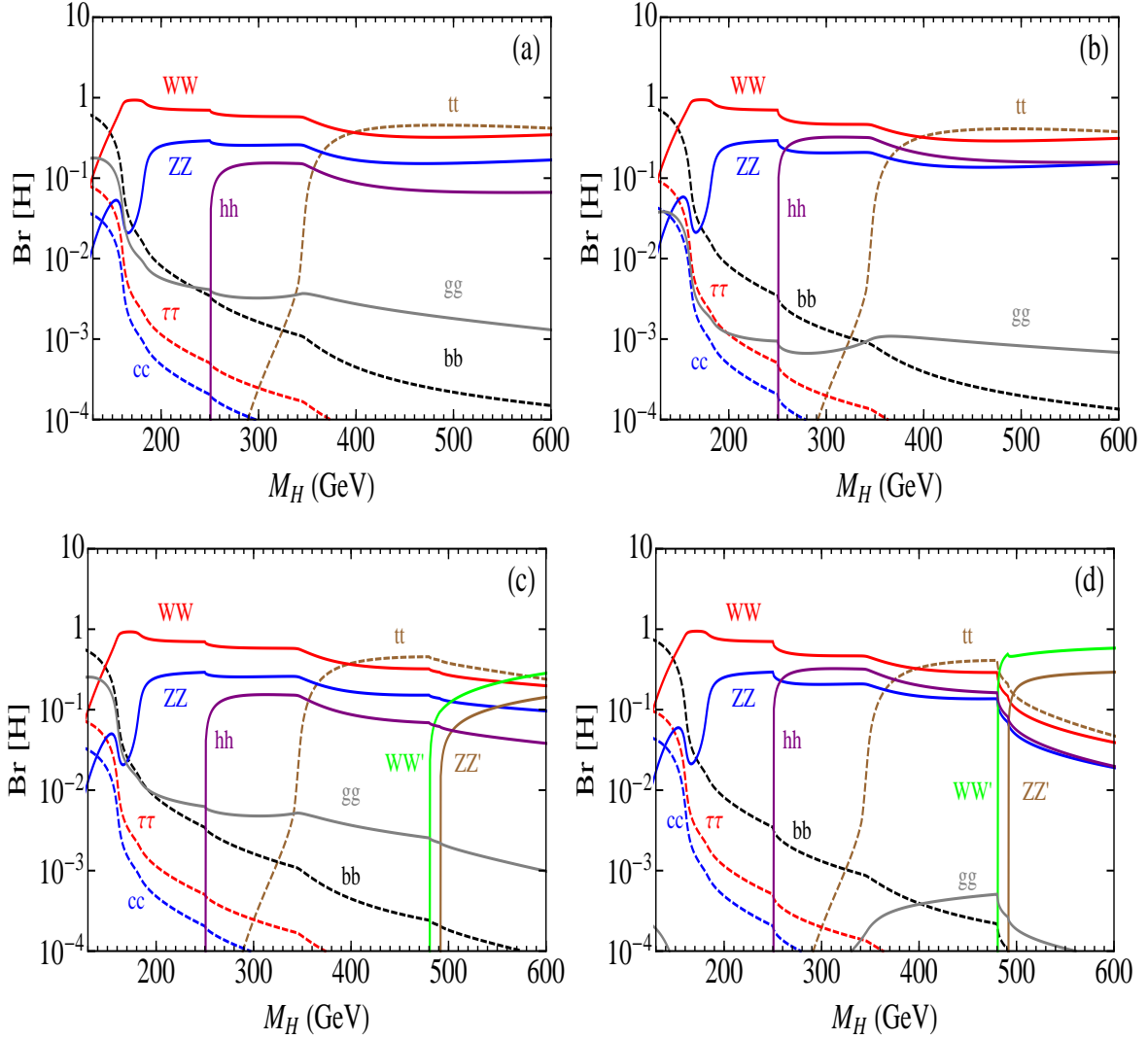


Figure 11. Decay branching fraction of the heavier Higgs boson H^0 of our model. We have inputs $r = 1$ and $M_F = 2.5$ TeV. The Higgs mixing angle is taken to be $\alpha = 0.6\pi$ for plot-(a)(c) and $\alpha = 0.8\pi$ for plot-(b)(d). We set the W' mass $M_{W'} = 600$ GeV for plot-(a)(b) and $M_{W'} = 400$ GeV for plot-(c)(d).

In parallel to Eq. (3.1), we can define the ratio \mathcal{R}_{ggH} of the gluon-fusion production cross sections for the heavy Higgs boson H over a hypothetical SM Higgs boson with the same mass,

$$\mathcal{R}_{ggH} \equiv \frac{\sigma[gg \rightarrow H]}{\sigma[gg \rightarrow h]_{\text{SM}}} = \frac{\Gamma[H \rightarrow gg]}{\Gamma[h \rightarrow gg]_{\text{SM}}}. \quad (4.3)$$

In Fig. 13, we also present this ratio \mathcal{R}_{ggH} as a function of the Higgs mixing angle α . We input the heavy Higgs mass, $M_H = 250$ GeV for plot-(a)(b), and $M_H = 500$ GeV for plot-(c)(d).

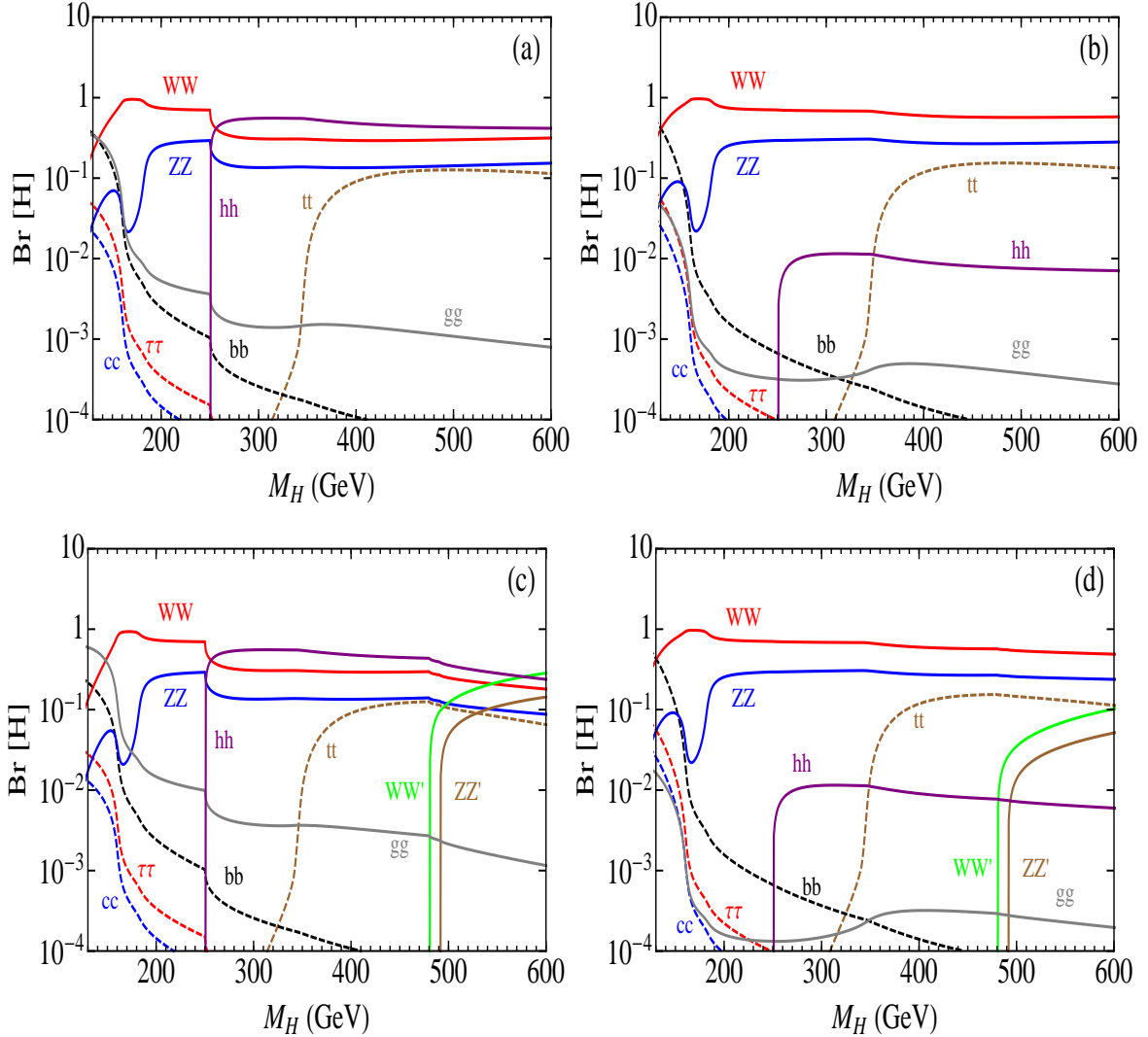


Figure 12. Decay branching fraction of the heavier Higgs boson H^0 of our model. We have input $r = \frac{1}{2}$ and $M_F = 2.5$ TeV. The Higgs mixing angle is taken to be $\alpha = 0.6\pi$ for plot-(a)(c) and $\alpha = 0.8\pi$ for plot-(b)(d). We set the W' mass $M_{W'} = 600$ GeV for plot-(a)(b) and $M_{W'} = 400$ GeV for plot-(c)(d).

The plots (a,c) and (b,d) have taken $M_{W'} = 400$ GeV and $M_{W'} = 600$ GeV, respectively. We also set the sample heavy fermion mass $M_F = 2.5$ TeV for all plots. From Fig. 13, we see that for the sample inputs of $r = (1, \frac{1}{2}, 2)$, the signal ratio \mathcal{R}_{ggH} reaches its peak around $\alpha \simeq (0.15 - 0.35)\pi$, and falls into its minimum at $\alpha \simeq (0.7 - 0.9)\pi$. This should be compared to the production of the light Higgs boson h^0 as shown earlier in Fig. 7. The maximal and minimal values of the ratios \mathcal{R}_{ggH} (Fig. 13) and \mathcal{R}_{ggh} (Fig. 7) have different locations because the corresponding $H-t-\bar{t}$ and $h-t-\bar{t}$ Yukawa couplings in (2.25) depend on the mixing angle α

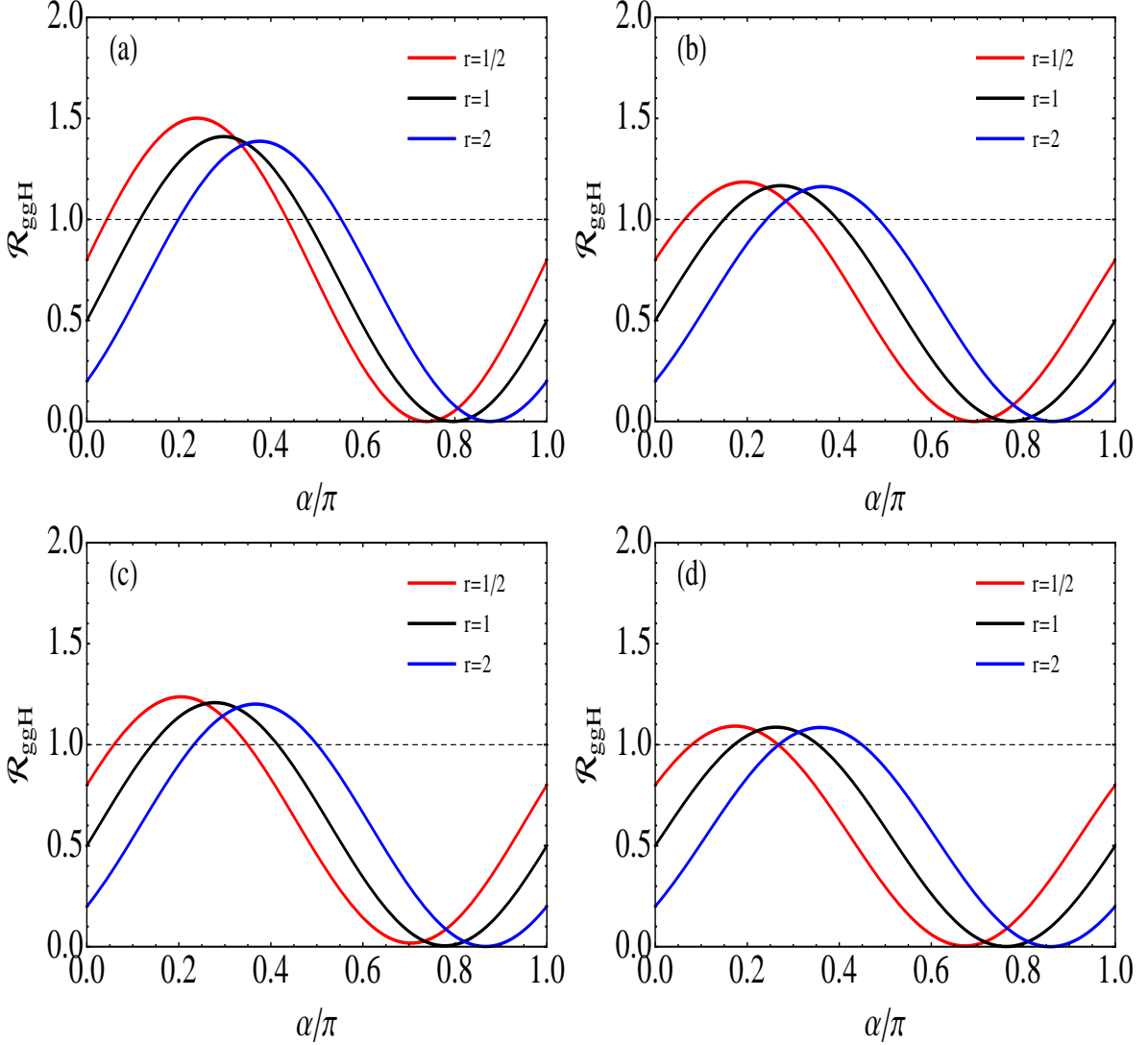


Figure 13. Ratio \mathcal{R}_{ggH} of H^0 production cross sections via gluon fusion process as a function of the Higgs mixing angle α . We set the heavy Higgs mass, $M_H = 250$ GeV for plot-(a)(b), and $M_H = 500$ GeV for plot-(c)(d). The plots (a,c) and (b,d) have $M_{W'} = 400$ GeV and $M_{W''} = 600$ GeV, respectively. All plots have input the heavy fermion mass $M_F = 2.5$ TeV.

differently.

4.2 LHC Potential of Detecting H^0

Next, we analyze the potential for probing the heavier Higgs boson H^0 at LHC. This is important for discriminating the present model from the conventional SM containing only one CP-even state h_{SM}^0 .

We study the LHC processes, $gg \rightarrow H^0 \rightarrow ZZ \rightarrow 4\ell$ and $gg \rightarrow H^0 \rightarrow WW \rightarrow 2\ell 2\nu$. Thus, we consider the following signal rates of H^0 over that of a hypothetical SM Higgs boson with the same mass,

$$\mathcal{R}_{ZZ} = \frac{\sigma(gg \rightarrow H) \times \text{Br}(H \rightarrow ZZ \rightarrow 4\ell)}{[\sigma(gg \rightarrow h) \times \text{Br}(h \rightarrow ZZ \rightarrow 4\ell)]_{\text{SM}}}, \quad (4.4a)$$

$$\mathcal{R}_{WW} = \frac{\sigma(gg \rightarrow H) \times \text{Br}(H \rightarrow WW \rightarrow 2\ell 2\nu)}{[\sigma(gg \rightarrow h) \times \text{Br}(h \rightarrow WW \rightarrow 2\ell 2\nu)]_{\text{SM}}}. \quad (4.4b)$$

We present our results in Fig. 14 with $r = 1$ and Fig. 15 with $r = 1/2$, respectively. In these two figures, we have also imposed the current 95% C.L. exclusions of ATLAS [31] and CMS [32] on the above signal ratios, shown as brown and black dashed curves. For the Higgs mixing angle in the range of $\alpha \lesssim 0.6\pi$, the LHC data have already put some nontrivial constraints on the H^0 mass below about 340 GeV. Especially, the parameter region around $\alpha = 0.25\pi$ is already largely excluded by the current data. This is expected since Fig. 13 shows that the production cross section of $gg \rightarrow H$ reaches its peak values around $\alpha \simeq (0.15 - 0.35)\pi$, and its minimal values around $\alpha \simeq (0.7 - 0.9)\pi$. It is useful to note that for the parameter region with a small mixing angle $\alpha \simeq (0.15 - 0.35)\pi$ is also disfavored by requiring the consistency of our light Higgs boson h^0 with the current LHC signals, as shown in Figs. 8-9.

From Figs. 14-15, we see that both signal ratios \mathcal{R}_{ZZ} and \mathcal{R}_{WW} decrease when the Higgs mixing angle increases from $\alpha = 0.25\pi$ to $\alpha = 0.8\pi$. In Fig. 14 with $r = 1$, for the h^0 signals become maximal around $\alpha = 0.8\pi$ (Fig. 8), the corresponding signals of the heavier H^0 Higgs boson via the (WW, ZZ) channels are much suppressed relative to the SM expectation, by a factor of $\mathcal{R}_{WW/ZZ} = \mathcal{O}(10^{-2})$ for $M_{W'} = 600$ GeV, and $\mathcal{R}_{WW/ZZ} = \mathcal{O}(10^{-2} - 10^{-3})$ for $M_{W'} = 400$ GeV. Thus, in this case the H^0 becomes hidden and escapes the current LHC detections. On the other hand, the situation gets changed for a mildly reduced Higgs mixing angle such as $\alpha = 0.6\pi$, for which we derive the corresponding signal rates for the light Higgs boson h^0 from Fig. 8,

$$\mathcal{R}_{\gamma\gamma} = 0.96, \quad \mathcal{R}_{ZZ} = 0.30, \quad \mathcal{R}_{WW} = 0.35, \quad (\text{for } M_{W'} = 400 \text{ GeV}), \quad (4.5a)$$

$$\mathcal{R}_{\gamma\gamma} = 0.82, \quad \mathcal{R}_{ZZ} = 0.25, \quad \mathcal{R}_{WW} = 0.27, \quad (\text{for } M_{W'} = 600 \text{ GeV}). \quad (4.5b)$$

In these samples, the $\gamma\gamma$ rates are slightly lower than the SM expectation, and the ZZ^* and WW^* signals are about a factor 1/3 of the SM. These are still consistent with the current ATLAS and CMS observations [3, 4] shown in Fig. 8 [Sec. 3.2]. In the meantime, the current experimental data from both ATLAS and CMS are still insufficient to discover or exclude such a non-SM Higgs boson H^0 with $\alpha \gtrsim 0.6\pi$. An increase of the integrated luminosity up to $\mathcal{L}_{\text{tot}} = 40 - 60 \text{ fb}^{-1}$ at the LHC (8 TeV) for both detectors should provide more effective probe of H^0 in this case. The next phase of the LHC (14 TeV) with an integrated luminosity of 100 fb^{-1} will do a much better job for detecting such a heavy Higgs boson H^0 .

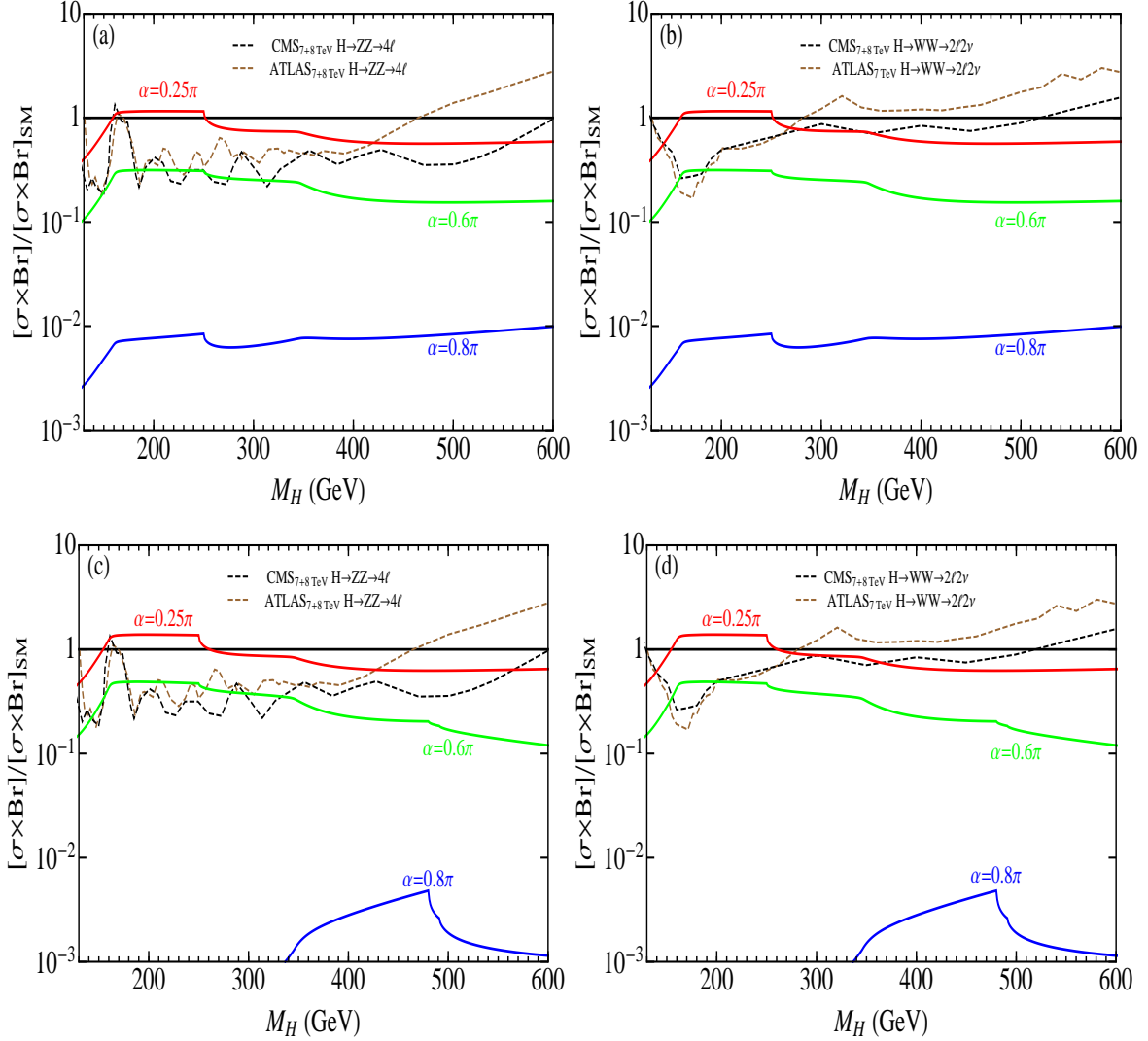


Figure 14. Signal ratios \mathcal{R}_{ZZ} and \mathcal{R}_{WW} for the heavy Higgs boson searches at the LHC. Plots (a) and (c) present the ratio \mathcal{R}_{ZZ} , while plots (b) and (d) display the ratio \mathcal{R}_{WW} . We have input the W' mass $M_{W'} = 600$ GeV for plots (a)-(b), and $M_{W'} = 400$ GeV for plots (c)-(d). The other inputs are taken to be $r = f_2/f_1 = 1$, and $M_F = 2.5$ TeV. The blue, red, and green curves in each plot correspond to three different Higgs mixing angles, $\alpha = (0.8\pi, 0.6\pi, 0.25\pi)$, respectively. The 95% C.L. exclusion curves of ATLAS (brown dashed) and CMS (black dashed) are imposed for comparison.

Furthermore, Fig. 15 shows that the suppressions on the $H^0 \rightarrow WW, ZZ$ signals become moderate with $r = \frac{1}{2}$. We find that the heavy Higgs boson signal predictions with $\alpha = 0.8\pi$ are much larger than the corresponding Fig. 14 ($r = 1$), and become larger than (or comparable to) the case of $\alpha = 0.6\pi$ in Fig. 15 ($r = \frac{1}{2}$). Fig. 15 also shows that the signal

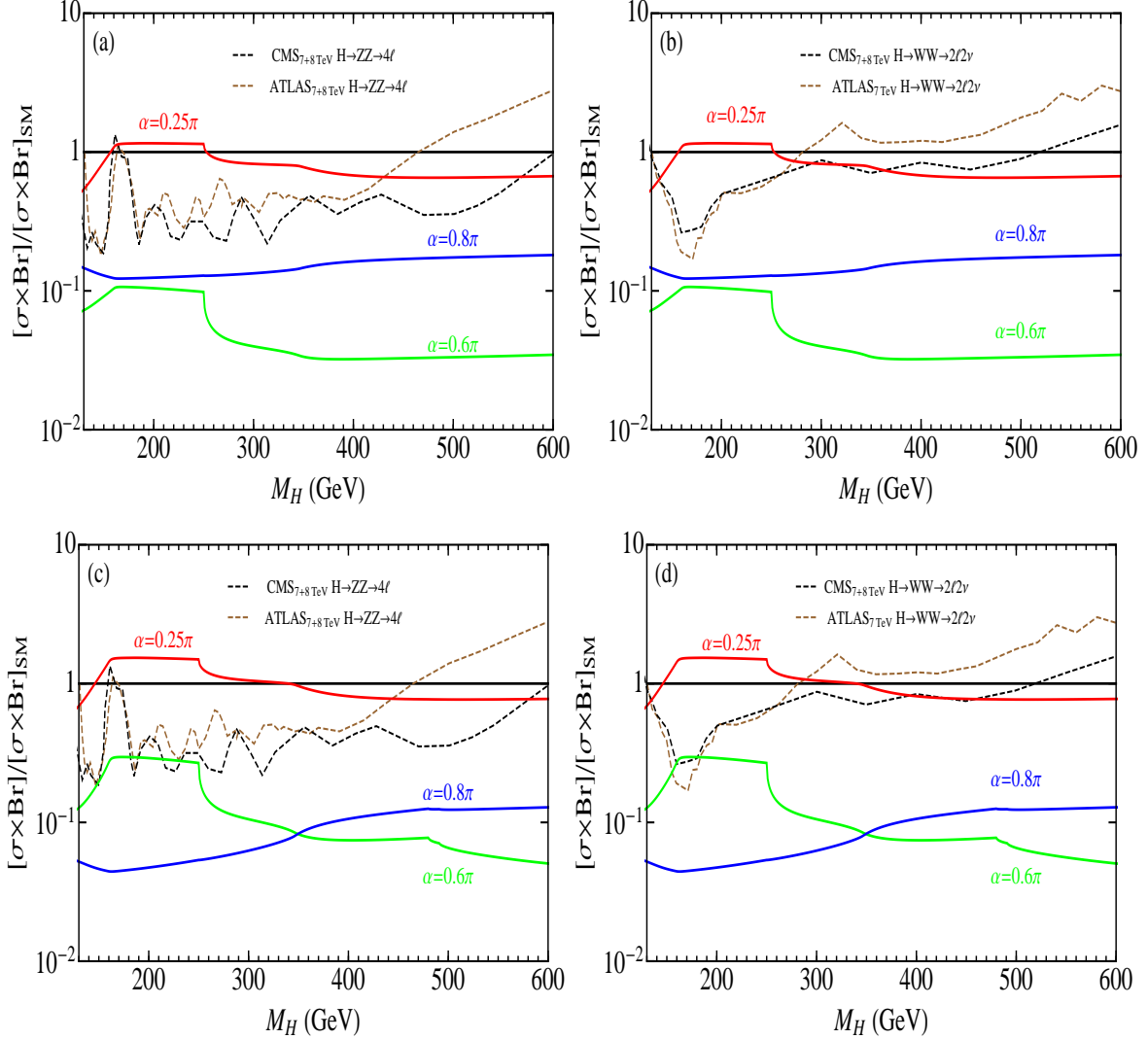


Figure 15. Signal ratios \mathcal{R}_{ZZ} and \mathcal{R}_{WW} for the heavy Higgs boson searches at the LHC. Plots (a) and (c) present the ratio \mathcal{R}_{ZZ} , while plots (b) and (d) display the ratio \mathcal{R}_{WW} . Different from Fig. 14, we have input $r = f_2/f_1 = 1/2$ for all plots. The W' mass is taken to be $M_{W'} = 600$ GeV for plots (a)-(b), and $M_{W'} = 400$ GeV for plots (c)-(d). The heavy fermion mass is $M_F = 2.5$ TeV. The blue, red, and green curves in each plot correspond to three different Higgs mixing angles, $\alpha = (0.8\pi, 0.6\pi, 0.25\pi)$, respectively. The 95% C.L. exclusion curves of ATLAS (brown dashed) and CMS (black dashed) are imposed for comparison.

rates with $\alpha = (0.6 - 0.8)\pi$ are within a factor of $\mathcal{O}(10)$ from the current LHC exclusion limits via the $H^0 \rightarrow ZZ \rightarrow 4\ell$ and $H^0 \rightarrow WW \rightarrow 2\ell 2\nu$ channels. Hence, we anticipate exciting search results of H^0 from the LHC (8 TeV) after analyzing the full data sample of

2012. Much more sensitive probes of H^0 will be done in the next phase of the LHC running at the 14 TeV collision energy.

Besides the major channels of $gg \rightarrow H^0 \rightarrow WW, ZZ$, we also note that the scalar channel $gg \rightarrow H^0 \rightarrow h^0 h^0 \rightarrow (b\bar{b})(b\bar{b})$ is also useful when $M_H > 2M_h \simeq 250$ GeV. Especially, the new CMS analysis shows that a b -tagging efficiency of 70% – 85% can be realized [33]. Thus, tagging the $4b$ final state only reduces our signal rate by a factor of $(24-52)\% \simeq \frac{1}{4} - \frac{1}{2}$. Such $4b$ final state is distinctive because we can require each pair of energetic $b\bar{b}$ jets to reconstruct the 125 GeV resonance of h^0 and the $4b$ jets to further reconstruct the heavy H^0 resonance. This should effectively suppress the SM backgrounds.

In addition, from (2.27a) we note that the HVV' coupling is enhanced by the factor $M_{V'}/v$. Thus, for H^0 in the mass-range $M_H > M_{V'} + M_V$, the decay channels $H^0 \rightarrow WW', ZZ'$ become dominant, as shown in Figs. 11-12. For the mass-range $M_H > M_{V'} + M_V$, it is useful to search for the decay channels $H \rightarrow W'W, Z'Z \rightarrow Z^0 W^+ W^- \rightarrow 3\ell + jj + \cancel{E}_T$, with distinctive tri-lepton signals plus dijets and missing E_T , where we have $Z \rightarrow \ell^+ \ell^-$ and $WW \rightarrow (\ell\nu)(jj)$ with $\ell = e, \mu$. Finally, we expect that more sensitive detections of H^0 should come from next runs of the LHC at the 14 TeV collision energy and with much higher integrated luminosities around 100 – 300 fb $^{-1}$. The future Linear Colliders (either ILC or CLIC) should help to make further precision probes of the H^0 signals.

Finally, we note that due to the ideal fermion delocalization [14], the W' couplings to the SM fermions vanish and Z' couplings with the light fermions are suppressed by $m_W/M_{W'}$. Thus, the major decay modes of (W', Z') gauge bosons are, $W' \rightarrow WZ$ and $Z' \rightarrow WW$, or $W' \rightarrow Wh$ and $Z' \rightarrow Zh$. The partial decay widths of $V' \rightarrow V_1 V_2$, with $V_1 V_2 = WZ (WW)$ for $V' = W' (Z')$ are derived as follows,

$$\Gamma[V' \rightarrow V_1 V_2] = \frac{G_{V'V_1V_2}^2 M_{V'}^3}{192\pi m_1^2} \left[\frac{M_{V'}^2 + 10m_{12}^2}{m_2^2} + \frac{m_{12}^4 + 8m_1^2 m_2^2}{M_{V'}^2 m_2^2} \right] \left[\left(1 - \frac{m_+^2}{M_{V'}^2}\right) \left(1 - \frac{m_-^2}{M_{V'}^2}\right) \right]^{\frac{3}{2}}, \quad (4.6)$$

with the masses $(m_1, m_2) = (m_{V_1}, m_{V_2})$, $m_{\pm} = m_1 \pm m_2$, and $m_{12}^2 = m_1^2 + m_2^2$. For the other partial decay width of $V' \rightarrow Vh$ with $V = W (Z)$ for $V' = W' (Z')$, we deduce the following,

$$\Gamma[V' \rightarrow Vh] = \frac{\xi_{hVV'}^2 m_V^2 M_{V'}}{12\pi v^2} \left[2 + \frac{(M_{V'}^2 + m_V^2 - M_h^2)^2}{4m_V^2 M_{V'}^2} \right] \left[1 + \frac{(M_h^2 - m_V^2)^2}{M_{V'}^4} - 2 \frac{m_V^2 + M_h^2}{M_{V'}^2} \right]^{\frac{1}{2}}. \quad (4.7)$$

Here the gauge couplings $G_{V'V_1V_2} = G_{W'WZ}, G_{Z'WW}$ and the Higgs-gauge couplings $\xi_{hVV'} = \xi_{hWW'}, \xi_{hZZ'}$ are given by (2.28) and (2.26), respectively.

Taking into account these two major channels, we present the decay branching fractions of W' in Fig. 16 by varying Higgs mixing angle $\alpha \in [0, \pi)$. It turns out that $\text{Br}[W' \rightarrow WZ] > \text{Br}[W' \rightarrow Wh]$ always holds over the full range of parameter α . In particular, we marked the ranges of the mixing angle α in yellow strips where the corresponding $h^0 \rightarrow \gamma\gamma$ signal

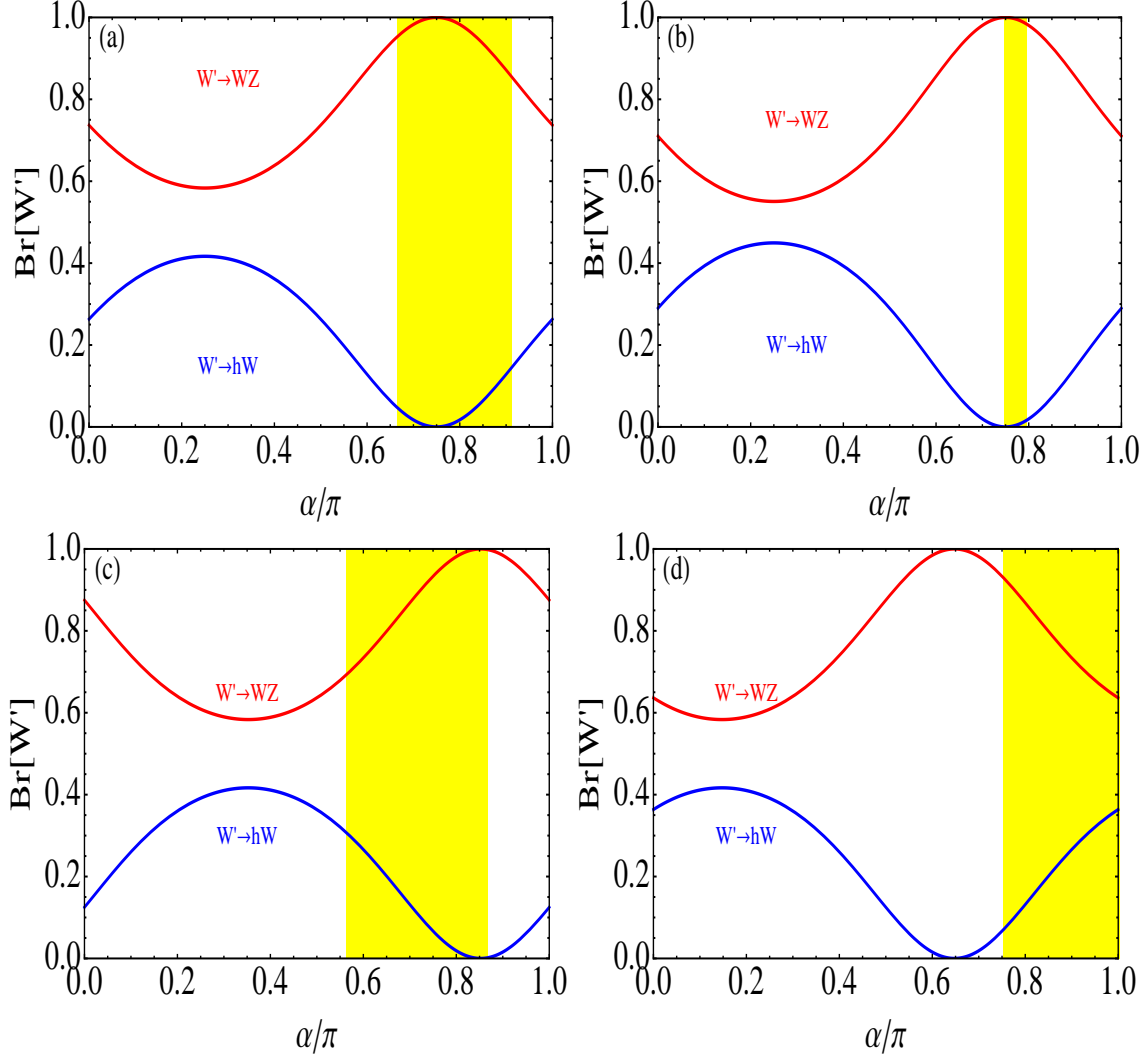


Figure 16. Decay branching fractions of W' versus Higgs mixing angle α for four sample inputs: $(r, M_{W'}) = (1, 400 \text{ GeV})$ [plot-(a)], $(r, M_{W'}) = (1, 600 \text{ GeV})$ [plot-(b)], $(r, M_{W'}) = (\frac{1}{2}, 400 \text{ GeV})$ [plot-(c)], and $(r, M_{W'}) = (2, 400 \text{ GeV})$ [plot-(d)]. The light Higgs boson mass $M_h = 125 \text{ GeV}$. The yellow strips correspond to the allowed α ranges by the consistency of our predicted $h^0 \rightarrow \gamma\gamma$ signals with the ATLAS/CMS data within $\pm 1\sigma$.

predictions (as shown in Fig. 8-9) are consistent with the ATLAS and CMS measurements within $\pm 1\sigma$. For such preferred parameter region of α , we see that the decay branching fraction $\text{Br}[W' \rightarrow Wh]$ is significantly suppressed relative to $\text{Br}[W' \rightarrow WZ]$. The situation for $\text{Br}[Z' \rightarrow Zh]$ versus $\text{Br}[Z' \rightarrow WW]$ is similar.

5 Conclusions

During the finalization of this paper, it is our pleasure to learn the LHC announcement on July 4, 2012 [3–6] of finding a Higgs-like new particle around 125 – 126 GeV. This has created great excitement to search for new physics of the Higgs sector and the origin of the electroweak symmetry breaking. Some other interesting theoretical interpretations have appeared very recently [34].

In this work, we have systematically studied the Higgs sector of a simple $SU(2) \otimes SU(2) \otimes U(1)$ gauge model (the 221 model), which has ideal fermion delocalization [14] and thus allows relatively light new gauge bosons (W', Z') below 1 TeV scale to participate in the unitarization of longitudinal $V_L V_L$ scattering ($V = W, Z$) together with the Higgs bosons (h, H). This may be viewed as an effective UV completion of the Higgsless 3-site nonlinear moose model [9]. In Sec. 2, we analyzed the structure of the model and derived all relevant Higgs, gauge and fermion couplings. Then, we derived the general sum rules (2.32)-(2.33) for the exact cancellation of asymptotic E^2 amplitudes of the longitudinal $V_L V_L$ scattering at high energies. From this we revealed that *such E^2 cancellations are achieved by the joint role of exchanging both spin-1 new gauge bosons and spin-0 Higgs bosons.* This was explicitly demonstrated in Fig. 1-2. We further derived the unitarity bound on the mass of the heavier Higgs state H^0 (Fig. 3) when the lighter Higgs boson h^0 weighs about 125 – 126 GeV.

In Sec. 3-4, we presented systematical analyses of the LHC phenomenology of the 221 model, focusing on the Higgs signatures in connection with the 125 – 126 GeV resonance h^0 and the probe of additional new Higgs state H^0 beyond the SM. We identified the lighter Higgs state h^0 with the LHC observed mass 125 GeV and set the Higgs VEV ratio $r = f_2/f_1 = \mathcal{O}(1)$ as input. The Higgs sector only contains two free parameters, namely, the heavier Higgs boson mass M_H and the Higgs mixing angle α . Hence, the parameter space of this model is highly predictive.

In Sec. 3, we analyzed the production of h^0 via gluon fusions and its decays via the most sensitive channels of $\gamma\gamma$, ZZ^* and WW^* , as shown in Figs. 4-7. The h^0 signal rates over the SM expectation are depicted in Figs. 8-9 via $\gamma\gamma$, ZZ^* , and WW^* channels. We found that due to new contributions of the heavy vector-like quarks in the current model the $gg \rightarrow h^0$ production rates can get enhanced for proper ranges of the Higgs mixing angle α (cf. Fig. 7). The maximal enhancements of the $\gamma\gamma$ rates are about a factor of 1.4 – 1.6 of the SM expectations, depending on the Higgs mixing angle α and the W' mass. The signal rates in the ZZ^* and WW^* channels are generally suppressed and can reach up to about 1/2 of the SM values for $r = 1$, and about a factor 0.8 – 1 of the SM for $r = \frac{1}{2}, 2$. These are compared with the current measurements of ATLAS [3] and CMS [4], and are found to reach good agreements. We further studied an interesting case with (nearly) degenerate h^0 and H^0 Higgs bosons around 125 – 126 GeV. As shown in Figs. 8-9 and Eqs. (3.3)-(3.4), we found that the predicted maximal $\gamma\gamma$ rates are higher than the SM by about 15% – 37% for $r = 1$ and 27% – 39% for $r = \frac{1}{2}, 2$, while the ZZ^* and WW^* signals can raise to about $\frac{1}{3} - \frac{1}{2}$ of the SM expectations for $r = 1$ and 58% – 93% of the SM for $r = \frac{1}{2}, 2$. They also

agree with the latest LHC findings [3, 4]. In addition, we studied the signal rates of h^0 via associate production and vector boson fusion channels, as shown in Fig. 10. It turns out that the predicted signals are generally suppressed by the tree-level hVV and hff couplings. For the VEV ratio f_2/f_1 varying within $\mathcal{O}(1)$, we found that the h^0 signal rates can reach up to about $\frac{1}{3} - \frac{3}{4}$ of the SM results. Hence, a combined analysis of h^0 signals in all three types of processes (including gluon fusions, Vh associate productions and vector boson fusions) will help to discriminate our h^0 Higgs boson from the SM.

In Sec. 4, we further analyzed the decays and productions of the heavier Higgs boson H^0 at the LHC. The detection of such a second new heavier H^0 state is important for discriminating the present model from the SM. The two major channels are $gg \rightarrow H^0 \rightarrow ZZ \rightarrow 4\ell$ and $gg \rightarrow H^0 \rightarrow WW \rightarrow 2\ell 2\nu$. The signal rates of H^0 over the SM expectations are shown in Figs. 14-15. The current search limits of ATLAS and CMS already start to probe H^0 via the ZZ and WW channels for the Higgs mixing angle $\alpha \lesssim 0.6\pi$ and mass-range below about 340 GeV. For the mixing angle in the $\alpha \sim (0.6 - 0.8)\pi$ range, the H^0 signal rates via ZZ and WW channels become lower and will require higher integrated luminosities at the LHC (14 TeV). But, in the mass-range $M_H > 250$ GeV, the decay mode $H^0 \rightarrow h^0 h^0$ may be sizable for $\alpha \sim 0.8\pi$ [Fig. 11(b)(d) with $r = 1$] or for $\alpha \sim 0.6\pi$ [Fig. 12(a)(c) with $r = \frac{1}{2}$]. Thus, the scalar channel $gg \rightarrow H^0 \rightarrow h^0 h^0 \rightarrow (b\bar{b})(b\bar{b})$ will be useful since it gives rise to the distinctive $4b$ final state with each pair of $b\bar{b}$ dijets reconstructing the 125 GeV resonance of h^0 . Furthermore, we note that in the mass-range $M_H > M_{W'} + m_W$, the H^0 Higgs state opens up new decay channels of $H^0 \rightarrow W'W, Z'Z \rightarrow Z^0 W^+ W^- \rightarrow 3\ell + jj + \cancel{E}_T$, with distinctive tri-lepton signals plus dijets and missing E_T , where $Z \rightarrow \ell^+ \ell^-$ and $WW \rightarrow (\ell\nu)(jj)$ with $\ell = e, \mu$. The $H^0 \rightarrow W'W/Z'Z$ modes may become the dominant decays for $M_H > M_{W'} + m_W$, as shown in Fig. 11(c,d) and Fig. 12(c,d). This is useful to give further probes of H^0 at the LHC.

Acknowledgments

We thank R. Sekhar Chivukula, Neil Christensen, and Masaharu Tanabashi for useful discussions. This research was supported by the NSF of China (under grants 11275101, 10625522, 10635030, 11135003) and the National Basic Research Program of China (under grant 2010CB833000). HJH thanks CERN Theory Division for hospitality during the finalization of this paper.

Appendices

A Decays of the Lighter Higgs Boson

In this Appendix A, we analyze all decay modes for the lighter Higgs boson h^0 in the present model, which will differ from the SM Higgs boson due to its non-standard couplings with gauge bosons and fermions shown in Sec. 2. There are three types of decay modes for h^0 ,

namely, (i) the weak gauge bosons WW/ZZ , (ii) the SM fermions, and (iii) the loop-induced radiative decay modes of $(gg, \gamma\gamma, Z\gamma)$.

The partial decay widths for $h \rightarrow VV$ ($V = W, Z$) final states differ from that of the SM Higgs boson by a common coupling factor according to Eq. (2.24),

$$\frac{\Gamma[h \rightarrow VV]}{\Gamma[h \rightarrow VV]_{\text{SM}}} \simeq \xi_{hVV}^2 \leq 1. \quad (\text{A.1})$$

This shows that the partial decay widths of h^0 to the weak gauge bosons tend to be smaller than the SM values. For h^0 decays into the SM fermions, the partial decay widths differ from the SM values by the corresponding Yukawa coupling factor as in Eq. (2.25),

$$\frac{\Gamma[h \rightarrow f\bar{f}]}{\Gamma[h \rightarrow f\bar{f}]_{\text{SM}}} \simeq \xi_{hff}^2 \leq 1, \quad (\text{A.2})$$

where f stands for a given SM fermion.

For the type (iii) loop-induced decay channels, there are two sources of the differences from the SM Higgs boson. One is the non-standard h^0 couplings to the SM particles, such as the hVV couplings in (2.24) and hff couplings in (2.25). The other source is the existence of extra new states, which enter the loop contributions. For the $h \rightarrow gg$ decays shown in Fig. 17, besides the top-quark, six new heavy vector-like partners of the SM quarks will also contribute to the loop. The decay width of $h \rightarrow gg$ differs the corresponding SM value by the ratio,

$$\frac{\Gamma[h \rightarrow gg]}{\Gamma[h \rightarrow gg]_{\text{SM}}} = \frac{\left| \sum_{f=t,Q} \xi_{hff} A_{1/2}^H(\tau_f) \right|^2}{\left| \sum_{f=t} A_{1/2}^H(\tau_f) \right|^2}, \quad (\text{A.3})$$

with $\tau_f \equiv m_h^2/(4m_f^2)$. The fermion-loop form factor is given by

$$A_{1/2}^H(\tau) = 2[\tau + (\tau - 1)f(\tau)]\tau^{-2}, \quad (\text{A.4a})$$

$$f(\tau) = \begin{cases} \arcsin^2 \sqrt{\tau}, & \tau \leq 1, \\ -\frac{1}{4} \left[\ln \frac{1 + \sqrt{1 - \tau^{-1}}}{1 - \sqrt{1 - \tau^{-1}}} - i\pi \right]^2. & \tau > 1. \end{cases} \quad (\text{A.4b})$$

In the heavy fermion mass limit $M_h^2 \ll 4m_f^2$, the asymptotic behavior is, $A_{1/2}^H(\tau) \rightarrow 4/3$. So, the loop contributions from the extra heavy quarks are comparable to that of the top-quark loop, and thus will enhance the Higgs production via the gluon fusion process. On the other hand, the coupling factors of the Higgs boson with the extra heavy fermions (2.26e) become, $\xi_{hQQ} = \mathcal{O}(m_W^2/M_{W'}^2) \ll 1$. Thus, the contributions from the heavy fermions

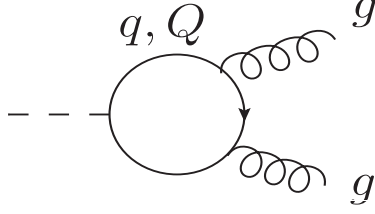


Figure 17. Loop-induced radiative decays of the light CP-even Higgs boson h^0 into gluon pairs, which include loop contributions from both the SM quarks q and new vector-like quarks Q in the present model.

only give moderate corrections to the Higgs productions, without drastic enhancement. This feature differs from other extensions, such as the fourth family SM fermions.

The modification to the $\Gamma[h \rightarrow \gamma\gamma]$ from the SM case is more complicated, since both fermion-loops and gauge-boson-loops enter this decay channel, as shown in Fig. 18. Schematically, the non-standard di-photon partial width of h^0 is expressed as follows at the leading order,

$$\frac{\Gamma[h \rightarrow \gamma\gamma]}{\Gamma[h \rightarrow \gamma\gamma]_{\text{SM}}} = \frac{\left| \sum_{f=t,Q} N_{c,f} Q_f^2 \xi_{hff} A_{1/2}^H(\tau_f) + \sum_{V=W,W'} \xi_{hVV} A_1^H(\tau_V) \right|^2}{\left| \sum_{f=t} N_{c,f} Q_f^2 A_{1/2}^H(\tau_f) + A_1^H(\tau_W) \right|^2}, \quad (\text{A.5a})$$

$$A_1^H(\tau) = -[2\tau^2 + 3\tau + 3(2\tau - 1)f(\tau)]\tau^{-2}, \quad (\text{A.5b})$$

where $N_{c,f} = 3(1)$ for colored (uncolored) states. Q_f denotes the electric charge for each fermion. $A_1^H(\tau)$ is the form factor of vector boson loop, with $\tau_V \equiv M_h^2/(4M_V^2)$. For the $h \rightarrow \gamma\gamma$ decay channel, there are both W -loops and W' -loops contributing to the partial decay width. The heavy vector boson limit of $M_h^2 \ll 4M_V^2$ gives the asymptotic behavior $A_1^H(\tau) \rightarrow -7$. Therefore, the contributions from the heavy gauge boson W' -loops can be compatible with the usual W -loop contribution. In most parameter space of this model, the pre-factor $\xi_{hW'W'}$ is not really suppressed, so the W' -loop contributions should be retained. Altogether, the $\Gamma[h \rightarrow \gamma\gamma]$ in this model can be comparable to that of the SM Higgs, even though $G_{hWW} \leq G_{hWW}^{\text{SM}}$ always holds. This feature differs from the case of $\Gamma[h \rightarrow WW/ZZ]$, which is always lower than the SM values.

The decay width $\Gamma[h \rightarrow Z\gamma]$ has similar feature to $\Gamma[h \rightarrow \gamma\gamma]$, and can be comparable to the SM values. But, in this radiative decay process, there are diagrams including both SM and heavy fields in the loop due to the existence of $G_{WW'h}$, $G_{WW'Z}$, and so on. We summarize all Feynman diagrams contributing to this decay channel in Fig. 19. The explicit formula for

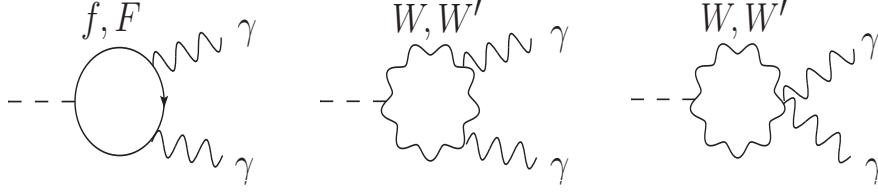


Figure 18. Loop-induced radiative decays of the light CP-even Higgs h^0 into di-photons in the present model.

$\Gamma[h \rightarrow Z\gamma]_{\text{SM}}$ contains contributions from the SM fermion-loops and the W -loops,

$$\Gamma[h \rightarrow Z\gamma]_{\text{SM}} = \frac{\alpha}{(4\pi)^3} \frac{M_h^3}{8\pi} \left(1 - \frac{m_Z^2}{M_h^2}\right)^3 \left| \mathcal{A}_{ff} + \mathcal{A}_{WW} \right|^2, \quad (\text{A.6a})$$

$$\mathcal{A}_{ff} \equiv \sum_f \frac{eN_{c,f}}{s_W c_W v} Q_f \hat{v}_f \mathcal{A}_{1/2}^H(\tau_f, \lambda_f), \quad (\text{A.6b})$$

$$\mathcal{A}_{WW} \equiv \frac{e}{s_W v} \mathcal{A}_1^H(\tau_W, \lambda_W), \quad (\text{A.6c})$$

with $\hat{v}_f = 2T_{3f} - 4Q_f s_W^2$ and Q_f denoting the electric charges. Here, the form factors are defined as,

$$\mathcal{A}_{1/2}^H(\tau, \lambda) \equiv I_1(\tau, \lambda) - I_2(\tau, \lambda), \quad (\text{A.7a})$$

$$\mathcal{A}_1^H(\tau, \lambda) \equiv c_W \left\{ 4 \left(3 - \frac{s_W^2}{c_W^2} \right) I_2(\tau, \lambda) + \left[(1 + 2\tau) \frac{s_W^2}{c_W^2} - (5 + 2\tau) \right] I_1(\tau, \lambda) \right\}. \quad (\text{A.7b})$$

where we have defined $\tau_i \equiv M_h^2/(4m_i^2)$ and $\lambda_i \equiv m_Z^2/(4m_i^2)$ for $i = f, V$. The relevant functions in the above form factors are defined as follows,

$$I_1(\tau, \lambda) = \frac{1}{2(\lambda - \tau)} + \frac{1}{2(\lambda - \tau)^2} \left[f(\tau) - f(\lambda) \right] + \frac{\lambda}{(\lambda - \tau)^2} \left[g(\tau) - g(\lambda) \right], \quad (\text{A.8a})$$

$$I_2(\tau, \lambda) = \frac{1}{2(\tau - \lambda)} \left[f(\tau) - f(\lambda) \right], \quad (\text{A.8b})$$

$$g(\tau) = \begin{cases} \sqrt{\tau^{-1} - 1} \arcsin \sqrt{\tau}, & \tau \leq 1, \\ -\frac{\sqrt{1-\tau^{-1}}}{2} \left[\ln \frac{1+\sqrt{1-\tau^{-1}}}{1-\sqrt{1-\tau^{-1}}} - i\pi \right], & \tau > 1. \end{cases} \quad (\text{A.8c})$$

For the $h^0 \rightarrow Z\gamma$ decay channel in the present model, the (A.6a) should be corrected by including all loop contributions given in Fig. 19. Analytically, we can express this partial decay width,

$$\Gamma[h \rightarrow Z\gamma] = \frac{\alpha}{(4\pi)^3} \frac{M_h^3}{8\pi} \left(1 - \frac{m_Z^2}{M_h^2}\right)^3 \left| \mathcal{A}_{ff} + \mathcal{A}_{FF} + \mathcal{A}_{fF} + \sum_{V=W, W'} \mathcal{A}_{VV} + \mathcal{A}_{WW'} \right|^2, \quad (\text{A.9})$$

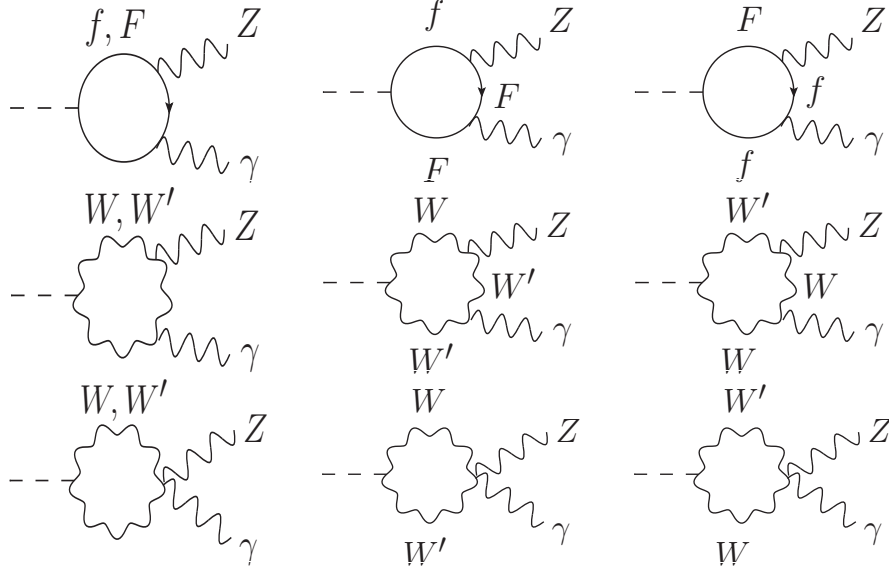


Figure 19. Loop-induced radiative decays of the light CP-even Higgs boson h^0 into the $Z\gamma$ final state in the present model.

where all the form factors read as follows,

$$\mathcal{A}_{ff} = \xi_f Q_f \hat{v}_f N_{c,f} \frac{e}{s_W c_W v} \mathcal{A}_{1/2}^H(\tau_f, \lambda_f), \quad (\text{A.10a})$$

$$\mathcal{A}_{FF} = \xi_F Q_F \hat{v}_F N_{c,F} \frac{e}{s_W c_W v} \mathcal{A}_{1/2}^H(\tau_F, \lambda_F), \quad (\text{A.10b})$$

$$\begin{aligned} \mathcal{A}_{fF} \simeq & \frac{4m_f}{M_F^2} \left[g_{h\bar{F}_R f_L} g_{\bar{F}_L f_L Z} + (L \leftrightarrow R) \right] \left(3 + 4 \ln \frac{m_f}{M_F} \right) \\ & - \frac{4}{M_F} \left[g_{h\bar{f}_R F_L} g_{\bar{f}_L F_L Z} + (L \leftrightarrow R) \right], \end{aligned} \quad (\text{A.10c})$$

$$\mathcal{A}_{WW} = \frac{e}{s_W v} \xi_{hVV} \mathcal{A}_1^H(\tau_W, \lambda_W), \quad (\text{A.10d})$$

$$\mathcal{A}_{W'W'} = \frac{e}{s_W v} \xi_{hV'V'} \mathcal{A}_1^H(\tau_{W'}, \lambda_{W'}), \quad (\text{A.10e})$$

$$\begin{aligned} \mathcal{A}_{WW'} \simeq & \frac{e}{s_W v} \xi_{hVV'} \frac{r}{1+r^2} \left[\frac{7}{2} + \frac{1}{18M_{W'}^2} (5M_h^2 \right. \\ & \left. - 45m_W^2 - 47m_Z^2 + 324m_W^2 \ln \frac{M_{W'}}{m_W}) \right]. \end{aligned} \quad (\text{A.10f})$$

In the above, we have taken both heavy fermions mass limit $M_F \gg (M_h, m_f, m_Z)$, and heavy W' mass limit $M_{W'} \gg (M_h, m_W, m_Z)$.

B Decays of the Heavier Higgs Boson

In this Appendix B, we further analyze the dominant decay modes for the heavy Higgs boson H^0 in the present model. For the LHC analysis in Sec. 4, we mainly consider H^0 for the mass-range of $M_H = 130 - 600$ GeV. The major decay modes of H^0 include, $H^0 \rightarrow WW, ZZ, WW', ZZ', t\bar{t}, b\bar{b}, \tau\bar{\tau}$.

The partial decay widths for $H^0 \rightarrow WW, ZZ$ channels differ from the SM values by a common coupling factor according to Eq. (2.24),

$$\frac{\Gamma[H \rightarrow VV]}{\Gamma[H \rightarrow VV]_{\text{SM}}} \simeq \xi_{HVV}^2 \leq 1, \quad (\text{B.1})$$

where $V = W, Z$. It shows that the partial width of $H^0 \rightarrow WW, ZZ$ tend to be smaller than the SM values. For the mass-range of $M_H > M_{V'} + m_V$ with $V' = W', Z'$, we have the new decay channels $H \rightarrow W'W, Z'Z$ opened. We derive these decay rates as,

$$\begin{aligned} \Gamma[H \rightarrow V'V] &= \frac{m_V^2 M_{V'}^2}{4\pi v^2 M_H} \xi_{HVV'}^2 \left(2 + \frac{(M_H^2 - M_{V'}^2 - m_V^2)^2}{4m_V^2 M_{V'}^2} \right) \\ &\times \sqrt{1 - 2\frac{m_V^2 + M_{V'}^2}{M_H^2} + \left(\frac{M_{V'}^2 - m_V^2}{M_H^2} \right)^2}. \end{aligned} \quad (\text{B.2})$$

Noting that the size of the dimensionless couplings $\xi_{HVV'}$ are comparable to the ξ_{HVV} , this decay width (B.2) are even enhanced over that of $H^0 \rightarrow WW, ZZ$, since we have, $\Gamma[H \rightarrow V'V]/\Gamma[H \rightarrow VV] \propto (M_{V'}/m_W)^2$. It is clear that the $H \rightarrow V'V$ can be the dominant decay modes once they are kinematically allowed, as shown in Fig. 12 of Sec. 4.1. For H^0 decays into the SM fermions, the partial decay widths differ from the SM Higgs values by the corresponding coupling factor as given in Eq. (2.25),

$$\frac{\Gamma[H \rightarrow f\bar{f}]}{\Gamma[H \rightarrow f\bar{f}]_{\text{SM}}} \simeq \xi_{Hff}^2 \leq 1, \quad (\text{B.3})$$

where f stands for the SM fermion.

Finally, the relevant loop-induced radiative decay channel $H \rightarrow gg$ in the present model also receives contributions from the six heavy vector-like partners of the SM quarks. This partial decay width differs from the corresponding SM value,

$$\frac{\Gamma[H \rightarrow gg]}{\Gamma[H \rightarrow gg]_{\text{SM}}} = \frac{\left| \sum_{f=t,Q} \xi_{Hff} A_{1/2}^H(\tau_f) \right|^2}{\left| \sum_{f=t} A_{1/2}^H(\tau_f) \right|^2}, \quad (\text{B.4})$$

where $\tau_f \equiv M_H^2/(4m_f^2)$.

References

- [1] F. Englert and R. Brout, Phys. Rev. Lett. **13** (1964) 321; P. W. Higgs, Phys. Rev. Lett. **13** (1964) 508; P. W. Higgs, Phys. Lett. **12** (1964) 132; G. S. Guralnik, C. R. Hagen and T. Kibble, Phys. Rev. Lett. **13** (1965) 585; T. Kibble, Phys. Rev. **155** (1967) 1554.
- [2] S. L. Glashow, Nucl. Phys. **22** (1961) 579; S. Weinberg, Phys. Rev. Lett. **19** (1967) 1264; A. Salam, in Elementary Particle Theory, Nobel Symposium No. 8, edited by N. Svartholm (Almqvist & Wiksells, Stockholm, 1968), p. 367.
- [3] F. Gianotti [ATLAS Collaboration], “Status of Standard Model Higgs Searches in ATLAS”, presentation at CERN, <http://indico.cern.ch/conferenceDisplay.py?confId=197461>, July 4, 2012.
- [4] J. Incandela, [CMS Collaboration], “Status of the CMS SM Higgs Search”, presentation at CERN, <http://indico.cern.ch/conferenceDisplay.py?confId=197461>, July 4, 2012.
- [5] G. Aad *et al.*, [ATLAS Collaboration], “Observation of a New Particle in Search for the Standard Model Higgs Boson with the ATLAS Detector at the LHC”, Phys. Lett. B **716** (2012) 1 [arXiv:1207.7214 [hep-ex]].
- [6] S. Chatrchyan *et al.*, [CMS Collaboration], “Observation of a New Boson at a Mass of 125 GeV with the CMS Experiment at the LHC”, Phys. Lett. B **716** (2012) 30 [arXiv:1207.7235 [hep-ex]].
- [7] N. Arkani-Hamed, A. G. Cohen and H. Georgi, Phys. Rev. Lett. **86** (2001) 4757 [arXiv:hep-th/0104005]; C. T. Hill, S. Pokorski and J. Wang, Phys. Rev. D **64** (2001) 105005 [arXiv:hep-th/0104035].
- [8] E.g., R. S. Chivukula, H. J. He, J. Howard and E. H. Simmons, Phys. Rev. D **69** (2004) 015009 [arXiv:hep-ph/0307209]; R. Foadi, S. Gopalakrishna, and C. Schmidt, JHEP **0403** (2004) 042 [arXiv:hep-ph/0312324]; R. S. Chivukula, E. H. Simmons, H. J. He, M. Kurachi, M. Tanabashi, Phys. Rev. D **70** (2004) 075008 [arXiv:hep-ph/0406077]; Phys. Rev. D **71** (2005) 115001 [arXiv:hep-ph/0502162]; E. Accomando, S. De Curtis, D. Dominici and L. Fedeli, Nuovo Cim. B **123** (2008) 809 [arXiv:0807.2951]; and references therein.
- [9] R. S. Chivukula, B. Coleppa, S. Di Chiara, E. H. Simmons, H. J. He, M. Kurachi, and M. Tanabashi, Phys. Rev. D **74** (2006) 075011 [arXiv:hep-ph/0607124].
- [10] A. Belyaev, R. S. Chivukula, N. D. Christensen, H. J. He, M. Kurachi, E. H. Simmons, and M. Tanabashi, Phys. Rev. D **80** (2009) 055022 [arXiv:0907.2662].
- [11] J. Pati and A. Salam, Phys. Rev. D **8** (1973) 1240; H. Georgi and S. L. Glashow, Phys. Rev. Lett. **32** (1974) 438; for a recent review, S. Raby, J. Phys. G **37** (2010) 075021 (p.193).
- [12] R. Casalbuoni, S. De Curtis, D. Dominici, R. Gatto, Phys. Lett. B **155** (1985) 95; R. Casalbuoni, A. Deandrea, S. De Curtis, D. Dominici, R. Gatto, and M. Grazzini, Phys. Rev. **D53** (1996) 5201 [arXiv:hep-ph/9510431].
- [13] M. Bando, T. Kugo, S. Uehara, K. Yamawaki, and T. Yanagida, Phys. Rev. Lett. **54** (1985) 1215; M. Bando, T. Kugo, and K. Yamawaki, Nucl. Phys. B **259** (1985) 493; M. Bando, T. Kugo, and K. Yamawaki, Prog. Theor. Phys. **73** (1985) 1541; M. Bando, T. Fujiwara, and K. Yamawaki, Prog. Theor. Phys. **79** (1988) 1140.

- [14] R. S. Chivukula, E. H. Simmons, H. J. He, M. Kurachi and M. Tanabashi, Phys. Rev. D **71** (2005) 115001 [arXiv:hep-ph/0502162]; Phys. Rev. D **72** (2005) 015008 [arXiv:hep-ph/0504114]; R. Casalbuoni, S. De Curtis, D. Dolce and D. Dominici, Phys. Rev. D **71** (2005) 075015 [arXiv:hep-ph/0502209].
- [15] G. Aad *et al.*, [ATLAS Collaboration], arXiv:1204.1648 [hep-ex]; T. Aaltonen *et al.*, [CDF Collaboration], Phys. Rev. D **83** (2011) 031102 [arXiv:1012.5145 [hep-ex]]; T. Aaltonen *et al.*, [CDF Collaboration], Phys. Rev. Lett. **102** (2009) 091805 [arXiv:0811.0053 [hep-ex]]; V. M. Abazov *et al.*, [D0 Collaboration], Phys. Lett. B **699** (2011) 145 [arXiv:1101.0806 [hep-ex]].
- [16] C. Du, H. J. He, Y. P. Kuang, B. Zhang, N. D. Christensen, R. S. Chivukula, E. H. Simmons, Phys. Rev. D **86**, 095011 (2012) [arXiv:1206.6022]; H. J. He, Y. P. Kuang, Y. Qi, B. Zhang, A. Belyaev, R. S. Chivukula, N. D. Christensen, A. Pukhov, E. H. Simmons, Phys. Rev. D **78** (2008) 031701 [arXiv:0708.2588]; T. Ohl and C. Speckner, Phys. Rev. D **78** (2008) 095008 [arXiv:0809.0023]; T. Abe, T. Masubuchi, S. Asai, and J. Tanaka, Phys. Rev. D **84** (2011) 055005 [arXiv:1103.3579]; F. Bach and T. Ohl, Phys. Rev. D **85** (2012) 015002 [arXiv:1111.1551].
- [17] X. Li and E. Ma, Phys. Rev. Lett. **47** (1981) 1788.
- [18] H. Georgi, E. E. Jenkins and E. H. Simmons, Phys. Rev. Lett. **62** (1989) 2789; Nucl. Phys. B **331** (1990) 541.
- [19] H. J. He, T. M. P. Tait, C. P. Yuan, Phys. Rev. D **62** (2000) 011702 (R) [hep-ph/9911266].
- [20] T. Jezo, M. Klasen, and I. Schienbein, arXiv:1203.5314 [hep-ph], and references therein.
- [21] T. Abe, R. S. Chivukula, E. H. Simmons, M. Tanabashi, Phys. Rev. D **85** (2012) 035015 [arXiv:1109.5856].
- [22] M. E. Peskin and T. Takeuchi, Phys. Rev. Lett. **65** (1990) 964; Phys. Rev. D **46** (1992) 381.
- [23] J. M. Cornwall, D. N. Levin, and G. Tiktopoulos, Phys. Rev. Lett. **30** (1973) 1268; Phys. Rev. D **10** (1974) 1145; C. H. Llewellyn Smith, Phys. Lett. **46B** (1973) 233. D. A. Dicus and V. S. Mathur, Phys. Rev. D **7** (1973) 3111; B. W. Lee, C. Quigg, and H. B. Thacker, Phys. Rev. Lett. **38** (1977) 883; Phys. Rev. D **16** (1977) 1519; M. S. Chanowitz and M. K. Gaillard, Nucl. Phys. B **261** (1985) 379.
- [24] C. Csaki, C. Grojean, H. Murayama, L. Pilo and J. Terning, Phys. Rev. D **69**, 055006 (2004) [hep-ph/0305237]; C. Csaki, C. Grojean, L. Pilo and J. Terning, Phys. Rev. Lett. **92**, 101802 (2004) [hep-ph/0308038].
- [25] R. S. Chivukula, D. A. Dicus, H. J. He, Phys. Lett. B **525** (2002) 175 [hep-ph/0111016]; R. S. Chivukula and H. J. He, Phys. Lett. B **532** (2002) 121 [hep-ph/0201164]; R. S. Chivukula, D. A. Dicus, H. J. He, S. Nandi, Phys. Lett. B **562** (2003) 109 [hep-ph/0302263]; H. J. He, Int. J. Mod. Phys. A **20** (2005) 3362 [hep-ph/0412113]; R. S. Chivukula, E. H. Simmons, H. J. He, M. Kurachi, and M. Tanabashi, Phys. Rev. D **75** (2007) 035005 [hep-ph/0612070]; R. S. Chivukula, H. J. He, M. Kurachi, E. H. Simmons, and M. Tanabashi, Phys. Rev. D **78** (2008) 095003 [arXiv:0808.1682].
- [26] H. J. He and Z. Z. Xianyu, arXiv:1112.1028 [hep-ph].
- [27] A. Djouadi, J. Kalinowski, M. Spira, Comput. Phys. Commun. **108** (1998) 56 [hep-ph/9704448].
- [28] M. Carena, I. Low, and C. E. M. Wagner, arXiv:1206.1082 [hep-ph].

- [29] E.g., J. R. Espinosa, C. Grojean, and M. Muehlleitner, EPJ Web Conf. **28** (2012) 08004 [arXiv:1202.1286 [hep-ph]]; B. Bellazzini, C. Csaki, J. Hubisz, J. Serra and J. Terning, arXiv:1205.4032 [hep-ph]; and references therein.
- [30] J. F. Gunion, Y. Jiang, and S. Kraml, arXiv:1207.1545 [hep-ph].
- [31] ATLAS Collaboration, ATLAS-CONF-2012-060 (June 6, 2012), “Search for the standard model Higgs boson in the $H \rightarrow WW^{(*)} \rightarrow \ell\nu\ell\nu$ decay mode using multivariate techniques with 4.7 fb^{-1} of ATLAS data”; ATLAS-CONF-2012-092 (July 6, 2012), “Observation of an excess of events in the search for the standard model Higgs boson in the $H \rightarrow ZZ^{(*)} \rightarrow 4\ell$ channel with the ATLAS detector”; and ATLAS-CONF-2012-098 (July 18, 2012), “Observation of an excess of events in the search for the standard model Higgs boson in the $H \rightarrow WW^{(*)} \rightarrow \ell\nu\ell\nu$ channel with the ATLAS detector”; see web link, <http://cdsweb.cern.ch/record/1454675/files>
- [32] CMS Collaboration, CMS-PAS-HIG-12-017 (July 8, 2012), “Search for the standard model Higgs boson decaying to W^+W^- in the fully leptonic final state in pp collisions at $\sqrt{s} = 8 \text{ TeV}$ ”; and CMS-PAS-HIG-12-016 (July 9, 2012), “Evidence for a new state in the search for the standard model Higgs boson in the $H \rightarrow ZZ \rightarrow 4\ell$ channel in pp collisions at $\sqrt{s} = 7$ and 8 TeV ”; see web link, <http://cdsweb.cern.ch/record/1460424/files>
- [33] S. Chatrchyan *et al.*, [CMS Collaboration], “Identification of b -quark jets with the CMS experiment”, CERN-PH-EP/2012-262 and arXiv:1211.4462 [hep-ex].
- [34] For a partial list of some very recent studies on the implications of the LHC new announcement, *e.g.*, B. Bellazzini, C. Petersson, R. Torre, arXiv:1207.0803 [hep-ph]; I. Low, J. Lykken, and G. Shaughnessy, arXiv:1207.1093 [hep-ph]; H. S. Cheon and S. K. Kang, arXiv:1207.1083 [hep-ph]; P. P. Giardino, K. Kannike, M. Raidal, and A. Strumia, arXiv:1207.1347 [hep-ph]; T. Corbett, O. J. P. Eboli, J. Gonzalez-Fraile, and M. C. Gonzalez-Garcia, arXiv:1207.1344 [hep-ph]; A. Arbey, M. Battaglia, A. Djouadi, and F. Mahmoudi, arXiv:1207.1348 [hep-ph]; E. Hardy, J. March-Russell, and J. Unwin, arXiv:1207.1435 [hep-ph]; M. R. Buckley and D. Hooper, arXiv:1207.1445 [hep-ph]; J. Baglio, A. Djouadi, and R. M. Godbole, arXiv:1207.1451 [hep-ph]; J. F. Gunion, Y. Jiang, and S. Kraml, arXiv:1207.1545 [hep-ph]; J. Ellis and T. You, arXiv:1207.1693 [hep-ph]; M. Montull and F. Riva, arXiv:1207.1716 [hep-ph]; J. R. Espinosa, C. Grojean, M. Muhlleitner, and M. Trott, arXiv:1207.1717 [hep-ph]; D. Carmi, A. Falkowski, E. Kuflik, T. Volansky, and J. Zupan, arXiv:1207.1718 [hep-ph]; S. Akula, P. Nath, and G. Peim, arXiv:1207.1839 [hep-ph]; H. An, T. Liu, and L. T. Wang, arXiv:1207.2473 [hep-ph]; P. S. Bhupal Dev, R. Franceschini, and R. N. Mohapatra, arXiv:1207.2756 [hep-ph]; H. Baer, V. Barger, P. Huang, A. Mustafayev, X. Tata, arXiv:1207.3343 [hep-ph]; A. G. Cohen and M. Schmaltz, arXiv:1207.3495 [hep-ph]; S. Banerjee, S. Mukhopadhyay, and B. Mukhopadhyaya, arXiv:1207.3588 [hep-ph]; R. Sato, S. Shirai, and K. Tobioka, arXiv:1207.3608 [hep-ph]; J. Cao, Z. Heng, J. M. Yang, and J. Zhu, arXiv:1207.3698 [hep-ph]; A. Alves, A. G. Dias, E. Ramirez Barreto, C. A. de S. Pires, F. S. Queiroz, and P. S. Rodrigues da Silva arXiv:1207.3699 [hep-ph]; D. S. M. Alves, P. J. Fox, and N. J. Weiner, arXiv:1207.5499 [hep-ph].